Progress in Oceanography 199 (2021) 102708

Contents lists available at ScienceDirect

Progress in Oceanography

journal homepage: www.elsevier.com/locate/pocean

Ocean acidification state variability of the Atlantic Arctic Ocean around northern Svalbard

Elizabeth M. Jones [a,*], Melissa Chierici [a,b], Sebastian Menze [c], Agneta Fransson [d], Randi B. Ingvaldsen [c], Helene Hodal Lødemel [a]

[a] Institute of Marine Research, Tromsø, Norway
[b] Department of Arctic Geophysics, University Centre in Svalbard, Longyearbyen, Norway
[c] Institute of Marine Research, Bergen, Norway
[d] Norwegian Polar Institute, Tromsø, Norway

ARTICLE INFO

Keywords:
Marine carbonate system
Inorganic nutrients
Atmospheric CO_2 uptake
Sea ice
Atlantic Water
Atlantification

ABSTRACT

The Svalbard shelf and Atlantic Arctic Ocean are a transition zone between northward flowing Atlantic Water and ice-covered waters of the Arctic. Effects of regional ocean warming, sea ice loss and greater influence of Atlantic Water or "Atlantification" on the state of ocean acidification, i.e. calcium carbonate ($CaCO_3$) saturation (Ω) are yet to be fully understood. Anomalies in surface layer Ω for the climatically-vulnerable $CaCO_3$ mineral aragonite ($\Delta\Omega$) were determined by considering the variability in $\Omega_{aragonite}$ during late summer each year from 2014 to 2017 relative to the four-year average. Greatest sea ice extent and more Arctic-like conditions in 2014 resulted in $\Delta\Omega$ anomalies of −0.05 to −0.01 (up to 45% of total $\Delta\Omega$) as a result of lower primary production. Conversely, greater Atlantic Water influence in 2015 supplied the ice-free surface layer with nitrate, which prolonged primary production to drive $\Delta\Omega$ anomalies of 0.01 to 0.06 (up to 45% of total $\Delta\Omega$) in more Atlantic-like conditions. Additionally, dissolution of $CaCO_3$ increased carbonate ion concentrations giving $\Delta\Omega$ anomalies up to 0.06 (up to 52% of total $\Delta\Omega$). These processes enhanced surface water Ω, which ranged between 2.01 and 2.65 across the region. Recent sea ice retreat in 2016 and 2017 (rate of decrease in ice cover of ~4% in 30 days) created transitional Atlantic-Arctic conditions, where surface water Ω varied between 1.87 and 2.29 driven by $\Delta\Omega$ anomalies of −0.10 to 0.01 due to meltwater inputs and influence of Arctic waters. Anomalies as low as −0.12 from reduced $CaCO_3$ dissolution in 2016 further supressed Ω. Wind-driven mixing in 2017 entrained Atlantic Water with low Ω into the surface layer to drive large $\Delta\Omega$ anomalies of −0.15 (up to 58% of $\Delta\Omega$). Sea-ice meltwater provided a minor source of carbonate ions, slightly counteracting dilution effects. Ice-free surface waters were substantial sinks for atmospheric CO_2, where uptake of 20.5 mmol m^{-2} day^{-1} lowered surface water Ω. "Atlantification" could exacerbate or alleviate acidification of the Arctic Ocean, being highly dependent on the numerous factors examined here that are intricately linked to the sea ice-ocean system variability.

1. Introduction

The Arctic Ocean and adjoining seas are particularly sensitive to increases in atmospheric carbon dioxide (CO_2) and are likely to be the first areas to experience widespread ocean acidification. Ocean acidification is caused by the lowering of carbonate ion concentrations, [CO_3^{2-}], and a decrease in calcium carbonate mineral saturation (Ω) (Orr et al., 2005; Fabry et al., 2009; Doney et al., 2009). This sensitivity is due to the low temperatures and naturally low [CO_3^{2-}] in Arctic waters that result from increased freshwater inputs from melting sea ice, glacial meltwater, precipitation and river runoff (e.g., Chierici and Fransson, 2009; Yamamoto-Kawai et al., 2011; Fransson et al., 2013, 2015). Freshwater sources are low in total alkalinity (A_T), the natural buffer against acidity, and have a dilution effect that reduces [CO_3^{2-}] and thus lowers Ω when mixed with seawater. Melting sea ice exposes previously ice-covered surface waters to the atmosphere and enhances air-sea CO_2 uptake, which further decreases Ω (e.g., Bates et al., 2006; Fransson et al., 2013). Remineralisation of pelagic and terrestrial organic matter and advection of anthropogenic CO_2-rich Atlantic Water further suppress Ω in subsurface waters of the Arctic Ocean (Anderson

* Corresponding author.
E-mail address: elizabeth.jones@hi.no (E.M. Jones).

https://doi.org/10.1016/j.pocean.2021.102708

Available online 1 November 2021

et al., 2009; Ericson et al., 2014; Anderson & Macdonald, 2015; Ulfsbo et al., 2018). These processes enhance the vulnerability of the surface layer to acidification in shelf seas and seasonally ice-covered regions (e.g. Chierici and Fransson, 2009; Yamamoto-Kawai et al., 2009; Zhang et al., 2020). The freshwater-induced suppression of Ω occurs at a potentially faster rate than reductions in $[CO_3^{2-}]$ that result from the uptake of anthropogenic CO_2 by the surface ocean, e.g. surface waters in the Canadian Arctic Archipelago already became undersaturated in 2005 (Chierici and Fransson, 2009) and surface waters in the Canada Basin reached aragonite undersaturation by 2008 with decreases in Ω of up to 0.09 $year^{-1}$ attributed to melting sea ice and air-sea CO_2 uptake (Yamamoto-Kawai et al., 2009; Zhang et al., 2020). Wind-induced vertical mixing with subsurface high CO_2 waters in summer and autumn decreases $[CO_3^{2-}]$ and suppresses Ω in the surface layer (Chierici et al., 2011; Fransson et al., 2017).

The lowering of Ω for calcium carbonate ($CaCO_3$) bio-minerals calcite ($\Omega_{calcite}$) and aragonite ($\Omega_{aragonite}$) has important consequences for marine organisms (Feely et al., 2004; Orr et al., 2005). The Ω (Eqn. (1)) is determined from concentrations of calcium, $[Ca^{2+}]$, and carbonate, $[CO_3^{2-}]$, in ambient seawater and K_{SP}, which defines the solubility of $CaCO_3$ as a function of the temperature, salinity and pressure of the ambient seawater (Zeebe and Wolf-Gladrow, 2001).

$$\Omega = \left(\left[CO_3^{2-}\right] + \left[Ca^{2+}\right]\right)/K_{sp} \quad (1)$$

In addition to biotic minerals aragonite and calcite, another important $CaCO_3$ mineral in seasonally ice-covered environments is the abiotic $CaCO_3$ mineral ikaite ($CaCO_3 \cdot 6H_2O$) that is very unstable and found in forming sea ice under specific thermo-haline conditions (Dieckmann et al., 2010 and references therein). Sea ice is known to contain a dynamic pool of dissolved inorganic carbon (C_T) and A_T and during sea ice formation, ikaite precipitates within brines and may become trapped within the ice matrix. During melting of the sea ice, ikaite is released in the meltwater and dissolves to provide a source of A_T and increasing $[CO_3^{2-}]$ to exert a geochemical control on Ω in surface waters influenced by seasonal ice melt (Rysgaard et al., 2007, 2012; Fransson et al., 2013, 2017). When Ω becomes less than 1, seawater is undersaturated with respect to $CaCO_3$ and conditions become energetically costly for $CaCO_3$ formation and potentially corrosive to marine calcifiers (Feely et al., 2004; Doney et al., 2009). Aragonite is the less stable form of $CaCO_3$ compared with calcite due to its comparatively higher solubility (Mucci, 1983) and is the most vulnerable to ocean acidification. A key zooplankton species in Arctic food webs is the pteropod *Limacina helicina* that constructs aragonitic shells, which are known to be sensitive to ocean acidification (Comeau et al., 2009; Bednaršek et al., 2012; Lischka and Riebesell, 2012). For Ω below 1.4, critical threshold conditions are reached whereby *L. helicina* shell calcification can be significantly reduced and survival of the species is threatened (Bednaršek et al., 2012, 2019).

The Arctic Ocean and high latitude seas are experiencing rapid change due to atmospheric and oceanic warming, sea ice losses and increases in freshwater inputs, and increased influences of warm Atlantic waters (Wassmann and Reigstad, 2011; Onarheim et al., 2014; Polyakov et al., 2017). The Svalbard archipelago is one of the fastest warming and with rapidly retreating sea ice on a global scale (Asbjørnsen et al., 2020). Svalbard is located in the Atlantic Arctic where the Arctic Ocean is connected to the North Atlantic Ocean through deep Fram Strait and the shallow Barents Sea. Northward flowing Atlantic Water and the southward passage of Arctic waters are exchanged and mixed within these gateways (Spall, 2013; Rudels et al., 2015). Since the late 1990s, the Atlantic Water inflow to the Arctic has warmed (Beszczynska-Moller et al., 2012) and resulted in a shift to a more Atlantic-like marine environment (Polyakov et al., 2017), referred to as "Atlantification" (Årthun et al., 2012; Assmy et al., 2017; Lind et al., 2018).

Warming and increased extent of Atlantic derived waters in the Arctic Ocean (i.e., "Atlantification") is consistent with higher Atlantic Water temperatures further upstream and increased inflow of Atlantic Water (González-Pola et al., 2018; Tsubouchi et al., 2020). This has led to a loss in sea ice along the western and northern shelves of Svalbard (Polyakov et al., 2017; Onarheim et al., 2014; Carmack et al., 2015) and contributed to the degradation of numerous marine-terminating glaciers along the western coast of Svalbard (e.g. Ewertowski, 2014). This has implications for primary production and biogeochemical cycling through supply of nutrients and dissolved carbonate minerals that increase the buffer capacity, limiting acidification in the fjord waters (Fransson et al., 2015, 2016; Ericson et al., 2019a; 2019b; Hopwood et al., 2020). Highly productive blooms are annual features in the marginal ice zone (MIZ) and are strongly regulated by ice-ocean interactions and surface stratification (Sakshaug, 2004; Carmack et al., 2006; Wassmann et al., 2006; Assmy et al., 2017). The spring and summer blooms lead to intense cycling of nutrients and inorganic carbon and constitute strong sinks for atmospheric CO_2 over the Arctic shelves (Chen and Borges, 2009; Chierici et al., 2011, 2019; Henley et al., 2020). The timing of ice algal and phytoplankton blooms is important for primary production and the regional marine food webs (Søreide et al., 2010; Leu et al., 2011).

"Atlantification" and the northward advance of Atlantic Water delivers increased heat, nutrients, A_T and C_T to subsurface waters around Svalbard and the Atlantic-Arctic Ocean. These changes have been linked to increases in primary production (Reigstad et al., 2002; Torres-Valdés et al., 2013; Randelhoff et al., 2018) with implications for the marine ecosystem and biogeochemical cycling (Wassman et al., 2006; Arrigo and van Dijken, 2015; Tremblay et al., 2015; Neukermans et al., 2018; Chierici et al., 2019). Conversely, warming surface waters and more ice melt, increases stratification that reduces vertical mixing and therefore limits nutrient (re)supply from below, which could result in decreases in primary production (e.g. Slagstad et al., 2015). These processes will affect the drawdown of atmospheric CO_2 with implications for the marine carbon cycle in the region (Fransson et al., 2017; Chierici et al., 2019). In order to understand the impacts of oceanic warming, reductions in sea ice and encroaching "Atlantification" on the current and future state of ocean acidification, knowledge of the physical, biological and biogeochemical impacts on the water column must be realised. This study presents carbonate chemistry, macronutrients and hydrographic data from late summer (August/September) in four consecutive years from 2014 to 2017. During the study period, varying sea ice and oceanographic conditions were found along the Atlantic Water inflow pathway that extended from eastern Fram Strait, along the northern shelf of Svalbard, Hinlopen Strait and the MIZ in the Nansen Basin, Arctic Ocean. Inter-annual variability in pH, carbonate ion concentrations and the degree of $CaCO_3$ saturation determined the state of ocean acidification as governed by meltwater inputs, water mass mixing and biological processes. The aim of this study is to better understand the spatio-temporal variability and perturbations to the state of ocean acidification, unravelling the complexities through examining the concomitant and counteracting nature of different processes in the climatically vulnerable Atlantic-Arctic Ocean.

2. Methods and data

2.1. Study area

The western and northern shelves of Svalbard and the Atlantic Arctic Ocean are influenced by the inflow of Atlantic Water, southwestward flowing Arctic water and advected sea ice, and the perennial advance and retreat of the pack ice (Fig. 1a). The West Spitsbergen Current (WSC), a continuation of the North Atlantic Current, is a boundary current that transports Atlantic Water through Fram Strait and forms the major pathway for warm and saline Atlantic Water to enter the Arctic Ocean (Carmack et al., 2015; Renner et al., 2018). The WSC splits at the Yermak Plateau with the Svalbard Branch flowing at 400–500 m depth between the Yermak Plateau and Svalbard into the Nansen Basin

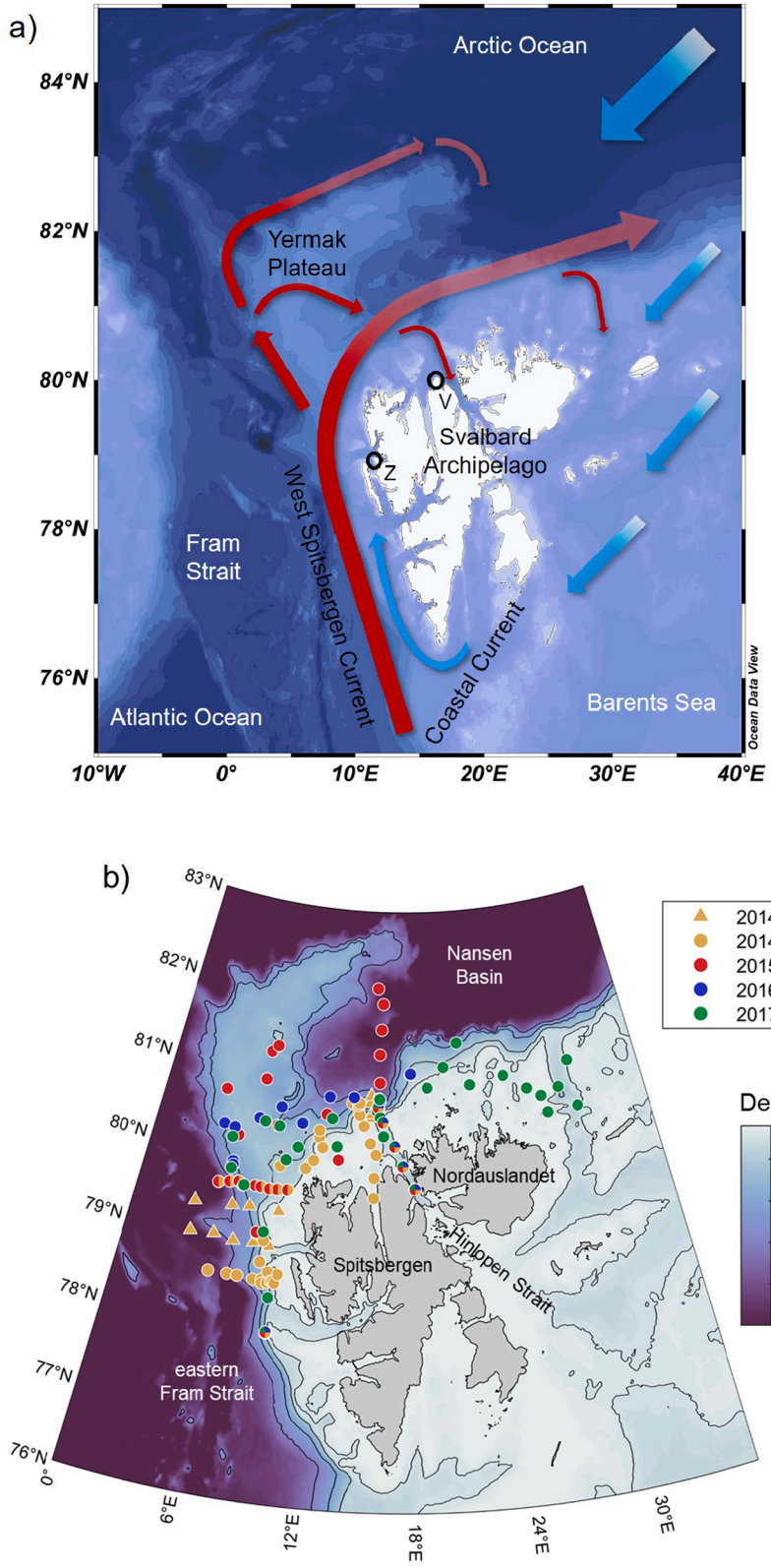

Fig 1. Maps of the Svalbard Archipelago and Atlantic Arctic Ocean region showing (a) regional circulation and major topographic features. Red arrows depict the Atlantic Water inflow in the West Spitsbergen Current in eastern Fram Strait and the Atlantic Water pathways around the Yermak Plateau as well as the northern edge of the Svalbard shelf (Sievaag and Fer, 2009; Menze et al. 2019). Blue arrows depict the general southward flow of Arctic waters and sea ice, and the westward flowing Coastal Current. Station locations in (b) during CarbonBridge 2014 (orange triangles), SI-ARCTIC 2014 (orange dots), SI-ARCTIC 2015 (red dots), SI-ARCTIC 2016 (blue dots) and SI-ARCTIC 2017 (green dots) and local topographic features are marked. Locations of Zeppelin Observatory (Z) and Verlegenhuken weather station (V) are marked (black circles) on Spitsbergen island, to the southwest of Nordauslandet island, separated by Hinlopen Strait in (a). Colour scale is depth with bathymetric data retrieved from the International Bathymetric Chart of the Arctic Ocean (Jakobsson et al., 2012) and isobaths marked in black at 500, 1000, 1500, 2000 and 2500 m in (b). Ocean Data View (Schlitzer R, 2015) is used as a data visualisation tool in (a) and Matlab toolbox m_map was used for mapping in (b). (For interpretation of the references to color in this figure legend, the reader is referred to the web version of this article.)

(Aagaard et al., 1987; Sievaag and Fer, 2009; Menze et al., 2019). The Yermak Branch flows around the western and northern slopes of the plateau at 1500 m depth and can become incorporated into the Svalbard Branch (Menze et al., 2019). Cold and fresh Arctic water is transported northwards around the Svalbard coast within the Coastal Current (e.g. Cottier et al., 2005). The Atlantic Water encounters the salinity-stratified Arctic waters and the seasonal ice pack to form a transition zone between Atlantic and Arctic oceanic environments (Rudels et al., 2015). This region is key for mixing and cooling of the Atlantic Water (Fer et al., 2015), which influences the local sea ice cover and seasonality of the MIZ, defined here as the area having an monthly average minimum of 15% ice concentration.

Water masses were classified (Table 1) based on the definitions given in Rudels et al. (2005) and Pérez-Hernández et al. (2017). The Atlantic Water is defined by potential temperature (θ) $\geq$ 0 °C and practical salinity $\geq$34.9 (Fig. 2), which is characterised here as a combination of Atlantic Water and Arctic Atlantic Water, as formed from cooled Atlantic Water. Definitions for Atlantic Water using sigma limitations ($27.70 < \sigma_\theta \leq 27.97$; Rudels et al., 2005) are not used here as part of the Atlantic Water had temperatures up to 8 °C. Interactions between Atlantic Water and sea-ice influenced Arctic waters form Polar Surface Water (PSW), which is the cold and low saline surface and halocline water that insulates the sea ice from the underlying Atlantic Water (Onarheim et al., 2014; Rudels et al., 2015). The ice meltwater and stratified PSW layer at and around the ice edge drive primary production and carbon uptake in the MIZ during spring and summer (Reigstad et al., 2002; Leu et al., 2011; Chierici et al., 2019). Warm Polar Surface Water (PSWw) is the warmer variety of PSW ($\theta > 0$ °C) formed by a combination of solar heating, sea ice melt and intrusions of Atlantic Water (Table 1). The temperature bound of 0 °C is used to delineate Atlantic Water and Arctic Intermediate Water (AIW), whereby the AIW occupies the depth range of 500–1600 m below the Atlantic Water (Fig. 2). The largest island of the archipelago, Spitsbergen, is separated from the island Nordaustlandet by a ~170 km long passage, the Hinlopen Strait (Fig. 1b). Within Hinlopen Strait is Hinlopen Trough, which extends from the northern mouth of the strait to the shelf break and enables Atlantic Water to intrude the northern shelf.

2.2. Oceanographic sampling

The Svalbard archipelago and Atlantic region of the Arctic Ocean was surveyed during four consecutive late summers (August/September) from 2014 to 2017 as part of the SI-ARCTIC (Strategic Initiative – The Arctic Ocean Ecosystem) project (Ingvaldsen et al., 2016a, 2016b, 2017a, 2017b). Additional hydrographic and biogeochemical sampling was carried out in August 2014 as part of the CarbonBridge project (Chierici et al., 2019 and references therein). Spatial surveys were carried out along the Atlantic Water inflow pathway that extends from eastern Fram Strait, along the northern shelf of Svalbard, Hinlopen Strait and into the MIZ of the Nansen Basin, Arctic Ocean. In 2015, the survey reached farther north in the thicker sea ice. In 2017, the survey extended farther east to cover the shallow shelf north of Nordaustlandet to about 30°E. The CarbonBridge survey was carried out 7–15 August 2014. SI-ARCTIC surveys were carried out from 15–20 August 2014, 18 August to 5 September 2015, 3–12 September 2016 and 22 August to 6 September 2017. The data are interpreted in the context of sea ice cover, freshwater inputs, different water masses, advection and mixing, biological production, calcium carbonate processes and air-sea CO_2 exchange, across the 4 main sub-regions.

Water samples were collected from 8-L Niskin bottles during CarbonBridge and 5-L Niskin bottles during SI-ARCTIC; Niskin bottles from both campaigns were mounted onto General Oceanics rosettes equipped with a conductivity-temperature-depth (CTD) sensor system (Seabird SBE-911 plus). Water was collected at typically 12 depths (e.g., 5, 10, 20, 30, 50, 100, 150, 200, then every 100 m to about 5–10 m above the seafloor) covering the water column at each hydrographic station, with higher resolution in the upper 100 m. The pycnocline and its strength were identified as the depth and value of the maximum Brunt–Väisälä frequency N^2, respectively.. Mixed layer depth (MLD) was set to be identical to the layer above the pycnocline (i.e., MLD = depth of maximum N^2), thereby ignoring any density gradients above the pycnocline. The MLD ranged between 3 m in freshwater-influenced Hinlopen Strait and 78 m in the deeply mixed water column in Fram Strait, with an average MLD of 20–22 m across all years. Therefore, 21 m is taken as an overall (average) representative MLD during the study period to ensure that it captures the variability in the seasonal stratification. A reference salinity of 35.07 ± 0.06 (S_{ref}; n = 42) determined from the average salinity for repeat stations in eastern Fram Strait for 2014–2017 (Fig. 1b) was used with the measured salinity (S) to estimate the freshwater fraction (FW) following Eq. (2).

$$FW = (S_{ref} - S)/S_{ref} \quad (2)$$

2.3. Meteorology, sea ice concentration and stable oxygen isotope of seawater

Wind speed, air pressure and air temperature data at 10 m height with a 6-hourly resolution for the month of September were obtained from the Norwegian Meteorological Institute (eklima.met.no/) from weather station Verlegenhuken (80.06 °N, 16.25 °E), north Spitsbergen (Fig. 1a). Relative to the 4-year study period (Table 2), 2014 had the strongest monthly mean winds of 7.4 ± 4.4 m s^{-1}, range of 0.5–19.7 m s^{-1}, and lowest air pressure of 1004 ± 9 mbar. Air temperatures were also colder −0.9 ± 2.4 °C in 2014 relative to the other years. In 2016,

Table 1
Water mass definitions based on potential temperature (θ, °C), practical salinity (S) and potential density (σ_θ, kg m^{-3}) and average, standard deviation, maximum and minimum values for all biogeochemical observations during the study period 2014–2017 (n = 1491): stable isotope of oxygen in seawater ($\delta^{18}O$,‰); nitrate (NO_3, µmol kg^{-1}); silicate ($Si(OH)_4$, µmol kg^{-1}); dissolved inorganic carbon (C_T, µmol kg^{-1}); total alkalinity (A_T, µmol kg^{-1}); pH on the total hydrogen ion scale(pH_T); carbonate ion concentration ($[CO_3^{2-}]$, µmol kg^{-1}); aragonite saturation state (Ω). *data from 2015, 2016, 2017 only. Water mass definitions derived from Rudels et al. (2005) and Pérez-Hernández et al. (2017): Polar Surface Water (PSW), warm Polar Surface Water (PSWw), Atlantic Water (AW), Arctic Intermediate Water (AIW). Number of data points (n) are in parentheses.

Water mass	Definition	$\delta^{18}O$ ‰*	NO_3 µmol kg^{-1}	$Si(OH)_4$ µmol kg^{-1}	C_T µmol kg^{-1}	A_T µmol kg^{-1}	pH_T	$[CO_3^{2-}]$ µmol kg^{-1}	Ω
Warm Polar Surface Water (PSWw) (n = 391)	$\theta > 0$	0.37	2.57 (3.27)	2.04 (1.18)	2072 (64)	2268 (54)	8.186	139 (17)	2.08
	$S < 34.9$	(0.26)	0.00	0.25	1880	2090	(0.065)	97	(0.28)
		-0.29	13.32	7.87	2178	2342	8.042	176	1.26
		1.16					8.376		2.65
Polar Surface Water (PSW) (n = 121)	$\sigma_\theta \leq 27.97$	0.28	3.20 (3.75)	1.91 (1.49)	2024 (98)	2205 (72)	8.254	128 (22)	1.92
	$\theta \leq 0$	(0.30)	0.00	0.00	1837	2039	(0.110)	93	(0.34)
		-0.73	12.48	5.59	2168	2291	8.048	172	1.29
		1.09					8.421		2.60
Atlantic Water (AW) (n = 863)	$\theta \geq 0$	0.55	10.07	4.41 (1.33)	2158 (19)	2317 (9)	8.071	116 (12)	1.68
	$S \geq 34.9$	(0.17)	(3.71)	0.24	2074	2297	(0.033)	97	(0.22)
		0.24	0.00	8.57	2189	2341	8.011	163	1.24
		1.10	14.68				8.211		2.46
Arctic Intermediate Water (AIW) (n = 118)	$\sigma_\theta > 27.97$	0.46	14.48	10.11	2167 (9)	2305 (6)	8.056	101 (3)	1.20
	$\theta < 0$	(0.14)	(0.99)	(1.85)	2142	2294	(0.015)	91	(0.10)
		0.29	11.73	4.81	2185	2325	8.098	107	0.98
		0.84	16.25	13.26			8.010		1.41

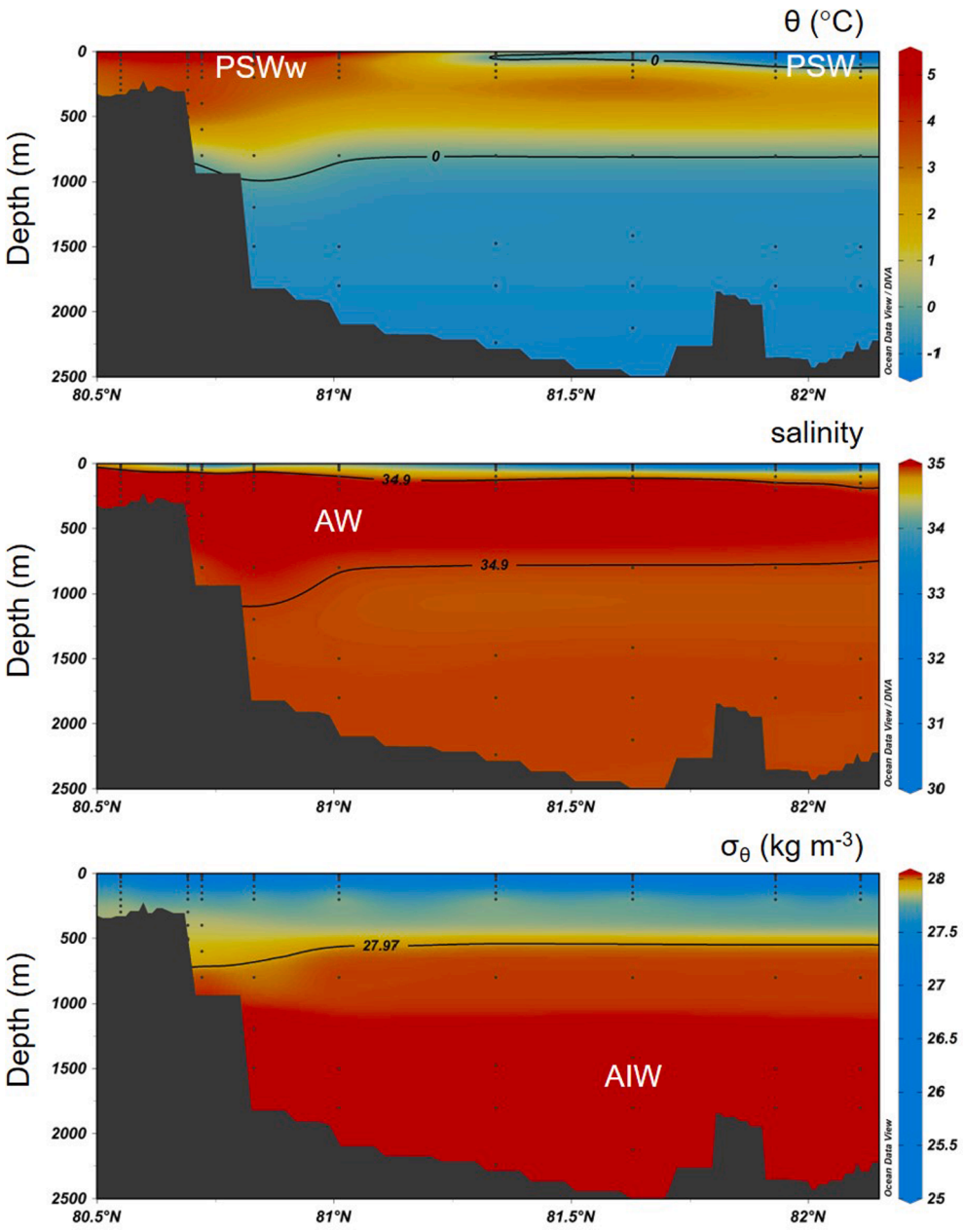

Fig 2. Section plots of potential temperature (θ, °C), salinity and potential density (σ_θ, kg m^{-3}) in the water column from the longest section extending from Hinlopen Strait, across the shelf and slope and into the Nansen Basin (SI-ARCTIC 2015). Key water mass boundaries are shown (black lines) for Polar Surface Water (PSW), warm Polar Surface Water (PSWw), Atlantic Water (AW), Arctic Intermediate Water (AIW) based on definitions from Rudels et al. (2005) and Pérez-Hernández et al. (2017). Black dots show sample positions. Ocean Data View (Schlitzer, 2015) is used as a data visualisation tool.

lowest wind speeds of 5.3 ± 3.6 m s^{-1}, ranging 0.3–14.2 m s^{-1}, occurred with an air pressure of 1007 ± 9 mbar and temperature was 1.7 ± 2.2 °C. September 2017 was characterised by the highest monthly mean air pressure of 1015 ± 8 mbar and warmest air temperatures 2.6 ± 2.7 °C, relative to the other years. Monthly mean wind speeds were similar in 2015 and 2017 at ~6.1 m s^{-1}, with strongest winds up to ~19 m s^{-1}.

Daily sea ice concentration data were derived from the Advanced Microwave Scanning Radiometer 2 (AMSR-2) products from the University of Bremen (seaice.uni-bremen.de, Spreen et al. 2008). Ice concentration data were gridded onto a stereographic grid and at each station location, the mean sea ice concentration in the last 30 days, linear trend in ice concentration in the last 30 days (if the r^2 of the fit was below 0.2 the trend was set to 0), number of ice covered days during the survey year and mean ice concentration in the survey year were determined.

Samples for determination of the stable oxygen isotopic ratio of seawater ($\delta^{18}O$) were collected in 2015, 2016 and 2017. Seawater was collected from the Niskin bottles into 25 mL vials and stored in the dark at 4 °C until analysis using a Thermo Fisher Scientific Delta V Advantage mass spectrometer with Gasbench II. Data were standardised relative to Vienna Standard Mean Ocean Water (VSMOW) for $\delta^{18}O$ (‰) with a reproducibility of replicate analyses of ±0.04‰. Higher $\delta^{18}O$ values are most isotopically enriched (heavier) with respect to ^{18}O and an indicator of oceanic and sea-ice meltwater (oceanic derived) water sources. Conversely, lower $\delta^{18}O$ values are most isotopically depleted (lighter) with respect to ^{18}O and an indicator of meteoric water sources. Origins of meteoric waters to the region are glacial meltwater and snow melt from localised influences of glaciers (isotopically light $\delta^{18}O$) in nearshore shelf waters and in Hinlopen Strait and sea ice (isotopically enriched $\delta^{18}O$) in the MIZ (Table 1).

2.4. Macronutrients and chlorophyll a

Samples for macronutrients nitrate + nitrite ($NO_3 + NO_2$), nitrite (NO_2) for determination of NO_3, phosphate (PO_4) and silicate ($Si(OH_4)$) were drawn from the Niskin bottles into 20 mL vials, preserved with

Table 2
Monthly (September) means and standard deviation of the meteorological variables wind speed (m s^{-1}), air pressure (mbar), air temperature and spatially averaged means in air-sea CO_2 variables ΔpCO_2 (µatm), air-sea CO_2 fluxes (mmol m^{-2} day^{-1}) and $\Delta C_{T\ flux}$ (µmol kg^{-1} $month^{-1}$) for 2014, 2015, 2016 and 2017. Number of observations (n) in parenthesis. The standard deviation in the air-sea CO_2 variables includes some spatial variability due to slight differences in sampling location across the region each year.

Variable	2014	2015	2016	2017
Wind speed (m s^{-1})	7.4 ± 4.4 (n = 89)	6.1 ± 3.5 (n = 120)	5.3 ± 3.6 (n = 105)	6.1 ± 4.0 (n = 120)
Air pressure (mbar)	1004 ± 9 (n = 97)	1009 ± 10 (n = 120)	1007 ± 9 (n = 119)	1015 ± 8 (n = 120)
Air temperature (°C)	−0.9 ± 2.4 (n = 104)	1.2 ± 1.9 (n = 120)	1.7 ± 2.2 (n = 120)	2.6 ± 2.7 (n = 120)
ΔpCO_2 (µatm)	−169 ± 44 (n = 12)	−158 ± 46 (n = 31)	−179 ± 35 (n = 16)	−180 ± 42 (n = 22)
Air-sea CO_2 fluxes (mmol m^{-2} day^{-1})	−20.4 ± 5.9 (n = 12)	−12.6 ± 4.0 (n = 31)	−11.1 ± 2.4 (n = 16)	−15.0 ± 3.7 (n = 22)
Air-sea CO_2 fluxes (ice scaled) (mmol m^{-2} day^{-1})	−13.3 ± 5.7 (n = 12)	−9.5 ± 2.8 (n = 31)	−8.6 ± 2.7 (n = 16)	−11.5 ± 3.3 (n = 22)
$\Delta C_{T\ flux}$ (µmol kg^{-1} $month^{-1}$)	21 ± 8 (n = 12)	13 ± 4 (n = 31)	12 ± 4 (n = 16)	16 ± 5 (n = 22)

chloroform and stored at 4 °C. Analysis was carried out at the Institute of Marine Research, Bergen, Norway, using a Flow Solution IV analyser from O.I. Analytical, United States, following Grasshof et al. (2009). The analyser was calibrated using reference seawater from Ocean Scientific International Ltd., United Kingdom. Samples for chlorophyll *a* (hereafter referred to as chlorophyll) were drawn from the Niskin bottles and were filtered over GF/F filters (0.45 µm mesh), placed in vials and frozen at −20 °C. All samples were extracted with methanol and analysed using a Turner 10-AU fluorometer (calibrated using chlorophyll, Sigma C6144) before and after acidification with 5% HCl at the Institute of Marine Research, Bergen, Norway.

2.5. Carbonate chemistry

Seawater samples for carbonate chemistry were drawn using Tygon tubing from Niskin bottles into 250 mL borosilicate glass bottles and either (i) stored for post-cruise analysis, where 60 µL of saturated mercuric chloride solution was added, at the Institute of Marine Research, Tromsø, in 2014, 2016 and 2017 or (ii) analysed onboard in 2015. Following methods outlined in Dickson et al. (2007), post-cruise determination of C_T was carried out by gas extraction of acidified (8.5% H_3PO_4) samples followed by coulometric titration and photometric detection (Johnson et al., 1987) using a Versatile Instrument for the Determination of Titration carbonate (VINDTA 3D, Marianda, Germany). Determination of A_T was carried out by potentiometric titration with 0.1 M hydrochloric acid in a semi-open cell using a Versatile Instrument for the Determination of Titration Alkalinity (VINDTA 3S, Marianda, Germany). Measurements were calibrated against Certified Reference Materials (CRM, provided by A. G. Dickson, Scripps Institution of Oceanography, USA) in 2014 (batch 139), 2016 (batch 160, 162, 164) and 2017 (batch 169, 170). The measurements precision, as determined from the average standard deviation for C_T and A_T replicate analyses, was within ±2 µmol kg^{-1}.

In 2015, determination of A_T and pH on the total hydrogen ion scale (pH_T) was performed directly onboard after a few hours thermostating to about 15 °C. The A_T was determined by potentiometric titration with 0.05 M hydrochloric acid in an open cell on a Metrohm Titrando system with a pH_T sensitive electrode with temperature measurements (Aquatrode). The accuracy of A_T was checked daily by analysis and correction based on CRM (batch 134), as detailed above. The pH_T was determined using a spectrophotometer (Agilent 8453 Diode-array) and pH sensitive dye (*meta*-cresol purple, 2 mM) and a 1 cm Quartz cuvette. 3 mL of the sample was mixed with 35 µL of the indicator dye. The pH_T of the indicator was measured daily using a 0.2 mm quartz cuvette and correction for the perturbation of the indicator pH_T was performed according to Chierici et al. (1999). The precision was performed on replicate analysis of samples and was for A_T about ±1 µmol kg^{-1}, and for pH_T ± 0.001.

Data consistency was checked using samples collected from the core of Atlantic Water (400–500 m) in eastern Fram Strait at 78.0 °N 9.5 °E (Fig. 1b), where repeat occupations from 2014 to 2017 during this study yielded measured and calculated (A_T, pH_T) values for C_T of 2165–2167 µmol kg^{-1}. These values are in very close agreement to C_T values of ~2167 µmol kg^{-1} reported previously at the corresponding depth range (Stöven et al. 2016). The mean age of the Atlantic Water in the upper 600 m in eastern Fram Strait, from transient tracer distributions by Stöven et al. (2016), was determined as 9 ± 10 years and therefore it is not expected that there would be an increase in C_T since the time of data collection in 2012 relative to the current study period.

2.6. Air-sea CO_2 fluxes

Air-sea CO_2 fluxes were calculated using the gas transfer velocity formula of Wanninkhof (2014), parameterized as a function of the Schmidt number (Sc) of the gas with the squared wind speed at 10 m above ground (U10), the solubility coefficient of CO_2 (K0) of Weiss (1974) and the gradient in pCO_2 between air and sea (ΔpCO_2sea-air). Monthly (September) mean squared wind speed from Verlegenhuken weather station (Fig. 1a) was used. Air xCO_2 (dry air) data were obtained from the Zeppelin Observatory (Fig. 1a), Spitsbergen (Norwegian Institute for Air Research; http://ebas.nilu.no/), as described in Ericson et al. (2019b). The atmospheric CO_2 concentrations were converted to partial pressures and fugacity by following the procedure in Dickson et al. (2007) using the monthly mean atmospheric pressure and the seawater vapor pressure calculated from the salinity and temperature of the surface waters (Ambrose and Lawrenson, 1972; Millero and Leung, 1976). Average monthly (September) pCO_2air in 2014, 2015, 2016 and 2017 was 380 ± 1 µatm, 384 ± 1 µatm, 388 ± 1 µatm, 389 ± 1 µatm, respectively.

The pCO_2sea in surface water (<10 m) was calculated from measured C_T and A_T (in 2014, 2016, 2017) and from measured pH_T and A_T (in 2015) using the CO_2-chemical speciation model CO2SYS accompanied by in situ temperature, salinity, pressure, PO_4 and $Si(OH)_4$ (Lewis and Wallace, 1998; van Heuven et al., 2011). The carbonic acid dissociation constants (pK_1 and pK_2) of Mehrbach et al. (1973) as refit by Dickson and Millero (1987) were selected as they have a good agreement with measured values in Arctic waters (Fransson et al., 2015; Chen et al. 2015; Woosley et al. 2017) and have been previously used for carbonate system studies along the Svalbard shelf region (Fransson et al., 2016, 2017; Chierici et al., 2019; Ericson et al., 2019b). A negative air–sea CO_2 flux implies a net transfer from the atmosphere into the ocean.

Sea ice can influence the air-sea CO_2 exchange (Butterworth and Miller, 2016), therefore the computed air-sea CO_2 fluxes were scaled to account for sea ice cover by applying a correction factor (100 minus the satellite derived sea ice concentration), following previous studies. This technique assumes that sea ice inhibits CO_2 exchange and that air-sea fluxes are a linear function of sea ice cover. However, it has been reported that sea ice allows a degree of air-sea CO_2 exchange (Semiletov et al., 2004; Loose et al., 2009). For 100% sea ice concentrations, the correction factor was adjusted to 1% to allow for any air-sea exchange that likely occurs due to breaking-up and melting of the ice pack, leads and brine channels, following previous studies (Bates et al., 2006; Shadwick et al., 2011; Fransson et al., 2017).

2.7. Ocean acidification state determination

2.7.1. pH and calcium carbonate saturation

Seawater pH_T, [CO_3^{2-}] and the $CaCO_3$ saturation state were

calculated from C_T and A_T (in 2014, 2016, 2017) and from measured pH_T and A_T (in 2015) using CO2SYS, as described in section 2.6. Changes in $[CO_3^{2-}]$ affect the solubility and degree of $CaCO_3$ saturation, which determines the Ω of $CaCO_3$ (aragonite and calcite) in the ocean (Eqn. (1)). In addition, freshwater from glacial melt and river runoff can supply surrounding seawater with dissolved minerals from weathering of the bedrock. Dissolution of carbonate-rich minerals dolomite $(CaMg(CO_3)_2)$ and $CaCO_3$ has been shown to increase A_T and enhance Ω in surface waters of Svalbard fjords (Fransson et al. 2015, 2016; Hopwood et al., 2020). The ocean acidification state is evaluated by consideration of the physical and biogeochemical processes that drive changes in $CaCO_3$ saturation, with reference to $[CO_3^{2-}]$ and pH_T. Hereafter, discussions on $CaCO_3$ saturation will focus on the more sensitive biomineral aragonite, unless otherwise stated, where $\Omega_{aragonite}$ is simplified to Ω.

2.7.2. Controls on surface water acidification states

The inter-annual variability in Ω in the mixed layer (upper 20 m) was investigated using anomalies ($\Delta\Omega = \Omega_{obs} - \Omega_{ave}$), which are derived from mean values in the upper 20 m in each observation year (Ω_{obs}) relative to the 4-year (2014–2017) average (Ω_{ave}). The anomalies are estimated using CO2SYS from variations C_T, A_T, $Si(OH)_4$, PO_4, salinity, temperature and pressure in the upper 20 m in each observation year relative to the 4-year average. Total ΔΩ was partitioned into effects of air-sea CO_2 fluxes, salinity changes, temperature changes, photosynthesis/respiration, calcium carbonate formation/dissolution, freshwater C_T and A_T supplies, advection and vertical mixing (Table 3) for each sub-region: (1) eastern Fram Strait, (2) northern shelf, (3) Hinlopen Strait and (4) the MIZ. Negative anomalies indicate a decrease in Ω in the observation year relative to the 4-year average and positive anomalies indicate an increase in the observation year relative to the 4-year average.

To account for the effects of oceanic CO_2 uptake on Ω, the corresponding rate of change in C_T (ΔC_Tflux; $\partial C_T/\partial t$, μmol kg^{-1} $month^{-1}$) was calculated using the daily ice-scaled fluxes summed for the month of September, divided by the seawater density in the upper 20 m. A positive ΔC_Tflux indicates increased C_T in the mixed layer. The $\Delta\Omega_{flux}$ was estimated by determining the anomaly in ΔC_Tflux for each sub-region and adding that value to the 4-year C_T average in the upper 20 m and using CO2SYS with the average A_T, $Si(OH)_4$, PO_4, salinity, temperature and pressure for each year to calculate the perturbed Ω for each observational year. The difference between the perturbed and 4-year average gives the change in Ω due to atmospheric CO_2 uptake by the ocean for each year per sub-region.

The effects of changes in salinity on Ω were investigated using CO2SYS with the average C_T, A_T, $Si(OH)_4$, PO_4, temperature and pressure for each year and the salinity anomaly ($S_{obs} - S_{ave}$) to calculate a perturbed Ω. The difference between the perturbed and 4-year average Ω gives the change in Ω due to salinity variations in the upper 20 m for each year per sub-region. The effects of temperature changes on Ω result from the thermodynamics of the carbonate system of seawater, where increased temperatures lead to increased $[CO_3^{2-}]$ and Ω (Pierrot et al., 2006). This was investigated using CO2SYS with the average C_T, A_T, Si $(OH)_4$, PO_4, salinity and pressure for each year and the temperature anomaly ($\theta_{obs} - \theta_{ave}$) to calculate a perturbed Ω. The difference between the perturbed and 4-year average gives the change in Ω due to temperature changes in the upper 20 m for each year per sub-region.

Photosynthetic uptake of CO_2 is accompanied by drawdown of NO_3, and an increase in A_T of 1 μmol kg^{-1} per 1 μmol NO_3 kg^{-1} drawn down during photosynthesis (Wolf-Gladrow et al., 2007). This results in an increase in $[CO_3^{2-}]$ and Ω. Conversely, remineralisation of organic matter from heterotrophic respiration releases CO_2 and NO_3, which reduces A_T, $[CO_3^{2-}]$ and Ω. The effects of biological CO_2 uptake on Ω was estimated from anomalies in $C_{T\ bio}$ (and corresponding $A_{T\ bio}$) calculated from anomalies in salinity normalised NO_3 ($NO_{3\ sal}$; Eq. (3)), i.e. $(NO_{3\ sal})_{obs} - (NO_{3\ sal})_{ave}$ and applying the Redfield C:N stoichiometric ratio (Redfield et al. 1963). This ratio was selected as a suitable estimate based on average C:N ratios of 6.7 and 7.9 in Atlantic and Arctic Water, respectively, in the Barents Sea (Frigstad et al. 2014). Salinity normalisation of nutrient concentrations (X) was carried out using the traditional method (Friis et al. 2003) using situ salinity (S) and the reference salinity (S_{ref}) following Eq. (3).

$$X_{sal} = (X/S) \times S_{ref} \quad (3)$$

The $\Delta C_{T\ bio}$ and $\Delta A_{T\ bio}$ were added to the average C_T and A_T in CO2SYS with the average $Si(OH)_4$, PO_4, salinity, temperature and pressure for each year to calculate a perturbed Ω. The change in Ω due to biological processes ($\Delta\Omega_{bio}$) was estimated from the difference between the perturbed Ω value and the 4-year average Ω.

The relationship between A_T and salinity is used to estimate the freshwater endmember, likely integrating signals from meteoric sources (glacial meltwater, snow melt, river runoff, rain) and melting sea ice, as previously used. The endmember estimates indicate that A_T and C_T of 186–360 μmol kg^{-1} and 226–364 μmol kg^{-1}, respectively, is released in freshwater to the upper 20 m across the sub-regions. The non-zero ΔA_T when $\Delta S = 0$ (Table 4) represents other processes affecting A_T, such as biological production (accounted for above), $CaCO_3$ formation/dissolution and terrestrial and benthic fluxes of A_T. Likely sources are from dissolution of $CaCO_3$ shells, for example from coccolithophores (Chierici et al., 2019; Oziel et al., 2020) and pteropods (Fransson et al., 2016 and references therein) that are ubiquitous across the shelf area, and from dissolving ikaite released from melting sea ice (Rysgaard et al., 2007; Fransson et al., 2013). In addition, glacial meltwater (Fransson et al., 2015; Ericson et al., 2019b) and riverine inputs (Cooper et al., 2008; Ericson et al. 2018) constitute supplies of A_T (and C_T) to surface waters. These sources of A_T provide a geochemical buffer and inputs of inorganic carbon in freshwater discharge to the Svalbard and the Atlantic Arctic Ocean. The freshwater fraction anomaly ($fw_{obs} - fw_{ave}$) was multiplied by the fraction of $A_{T\ S=0}$ and $C_{T\ S=0}$ based on the assumption that the A_T and C_T freshwater components (Table 4) are delivered to the upper 20 m at 100% freshwater fraction. The $\Delta C_{T\ fw}$ and $\Delta A_{T\ fw}$ were added to the average C_T and A_T and used in CO2SYS with the average $Si(OH)_4$, PO_4, temperature and pressure for each year to calculate a perturbed Ω. The change in Ω due to freshwater derived A_T and C_T ($\Delta\Omega_{FW}$) was estimated from the difference between the perturbed Ω value and the 4-year average Ω.

Changes in Ω resulting from $CaCO_3$ mineral (biotic aragonite and calcite; abiotic ikaite) formation or dissolution ($\Delta\Omega_{CaCO3}$) were determined from anomalies in potential A_T (A_T*; sum of salinity-normalised A_T and NO_3; Brewer and Goldman, 1976) and corresponding $C_{T\ CaCO3}$ in the ratio 2 ΔA_T: 1 ΔC_T (Zeebe and Wolf-Gladrow, 2001). Salinity

Table 3
Terminology used to investigate the inter-annual variability in ocean acidification. Anomalies (ΔΩ) in the aragonite saturation state (Ω) in the mixed layer are partitioned into changes resulting from air-sea CO_2 fluxes, salinity changes, temperature changes, photosynthesis/respiration, calcium carbonate formation/dissolution, freshwater derived C_T and A_T, advection and vertical mixing for each sub-region: (1) eastern Fram Strait, (2) northern shelf, (3) Hinlopen Strait and (4) the MIZ.

Acidification state terminology	Ω expression
in situ (determined from C_T, A_T)	Ω
observational year average	Ω_{obs}
4-year (2014–2017) average	Ω_{ave}
anomalies (total change)	$\Delta\Omega$ ($\Omega_{obs} - \Omega_{ave}$)
change due to air-sea CO_2 fluxes	$\Delta\Omega_{flux}$
change due to salinity changes	$\Delta\Omega_{sal}$
change due to temperature changes	$\Delta\Omega_{temp}$
change due to photosynthesis/respiration	$\Delta\Omega_{bio}$
change due to $CaCO_3$ formation/dissolution	$\Delta\Omega_{CaCO3}$
change due to freshwater derived C_T and A_T	$\Delta\Omega_{fw}$
change due to advection	$\Delta\Omega_{adv}$
change due to vertical mixing	$\Delta\Omega_{mix}$

Table 4
Relationships between physical and biogeochemical variables that effect the aragonite saturation (Ω) and drive perturbations in the ocean acidification state. Values are determined from all data during the 4-year study period (2014–2017) in the average depth of the mixed layer (upper 20 m) per sub-region. Rate of change in A_T with salinity (A_T/S); change in A_T versus change in salinity ($\Delta A_T/\Delta S$); value of A_T when salinity is 0 ($A_{T\ S=0}$); amount of change in A_T when change in salinity is 0 ($\Delta A_{T\ \Delta S=0}$); rate of change in C_T with salinity (C_T/S); value of C_T when salinity is 0 ($C_{T\ S=0}$); value of $\delta^{18}O$ when salinity is 0 ($\delta^{18}O_{\ S=0}$); average salinity in Atlantic Water (S_{AW}); average value of C_T in (Atlantic Water $C_{T\ AW}$); average value of Ω in Atlantic Water ($\Omega_{\ AW}$). Values estimated from linear regression relationships include relevant r^2, p value and number of observations (n) in parenthesis.

	Fram Strait	Northern shelf	Hinlopen Strait	MIZ
A_T/S, $\Delta A_T/\Delta S$	61.2 ± 2.7 (r^2 = 0.89; $p \ll 0.01$; n = 65)	61.1 ± 3.3 (r^2 = 0.91; $p \ll 0.01$; n = 36)	59.5 ± 1.7 (r^2 = 0.96; $p \ll 0.01$; n = 59)	55.7 ± 2.1 (r^2 = 0.90; $p \ll 0.01$; n = 80)
$A_{T\ S=0}$ (μmol kg^{-1})	192 ± 91 (r^2 = 0.89; p = 0.04; n = 65)	186 ± 111 (r^2 = 0.91; p = 0.10; n = 36)	241 ± 57 (r^2 = 0.96; $p < 0.01$; n = 59)	360 ± 68 (r^2 = 0.90; $p < 0.01$; n = 80)
$\Delta A_{T\ \Delta S=0}$ (μmol kg^{-1})	20 ± 2 (r^2 = 0.89; $p \ll 0.01$; n = 65)	1 ± 4 (r^2 = 0.91; p = 0.86; n = 36)	−6 ± 2 (r^2 = 0.96; $p < 0.01$; n = 59)	14 ± 2 (r^2 = 0.90; $p < 0.01$; n = 80)
C_T/S	52.4 ± 4.4 (r^2 = 0.70; $p \ll 0.01$; n = 64)	52.0 ± 4.0 (r^2 = 0.83; $p \ll 0.01$; n = 37)	49.6 ± 2.9 (r^2 = 0.84; $p < 0.01$; n = 59)	53.5 ± 3.1 (r^2 = 0.79; $p \ll 0.01$; n = 78)
$C_{T\ S=0}$ (μmol kg^{-1})	283 ± 150 (r^2 = 0.70; p = 0.06; n = 64)	283 ± 133 (r^2 = 0.83; p = 0.04; n = 37)	364 ± 96 (r^2 = 0.84; $p \ll 0.01$; n = 59)	226 ± 103 (r^2 = 0.79; p = 0.03; n = 78)
$\delta^{18}O_{\ S=0}$ (‰)	−1.52 ± 2.45 (r^2 = 0.05; p = 0.55; n = 12)	−3.30 ± 1.13 (r^2 = 0.41; $p < 0.01$; n = 18)	−5.59 ± 1.81 (r^2 = 0.24; $p < 0.01$; n = 36)	−0.88 ± 1.19 (r^2 = 0.03; p = 0.47; n = 38)
S_{AW}	35.06 ± 0.08	35.02 ± 0.07	35.00 ± 0.08	35.00 ± 0.09
$C_{T\ AW}$ (μmol kg^{-1})	2162 ± 26	2161 ± 10	2153 ± 14	2158 ± 16
Ω_{AW}	1.70 ± 0.29	1.60 ± 0.19	1.68 ± 0.18	1.60 ± 0.24

normalisation of C_T and A_T removes effects of changing salinity due to dilution and enrichment (Friis et al. 2003) and was carried out using the technique that accounts for the non-zero freshwater endmembers (Table 4). The resultant values were used in CO2SYS with the average C_T, A_T, $Si(OH)_4$, PO_4, salinity, temperature and pressure for each year to calculate a perturbed Ω. The change in Ω due $CaCO_3$ processes was estimated from the difference between the perturbed Ω value and the 4-year average Ω. Using changes in seawater C_T and A_T to estimate $\Delta\Omega_{CaCO3}$ cannot specify which $CaCO_3$ mineral is involved in the process.

The influence of advection ($\Delta\Omega_{adv}$; taken here to represent the horizonal exchange of water masses to differentiate from vertical mixing) of different water masses on Ω was estimated from relationships of C_T and A_T with salinity (Eqn. 4–5). For C_T, the relationship with salinity is non-conservative and therefore a theoretical mixing line between the freshwater endmember and Atlantic Water endmember is used per region (gradient #; Table 1) together with the average salinity in the upper 20 m per year, adapted from Ericson et al. (2019b). For A_T, the near-conservative relationship with salinity results in a dominant control on A_T and as such the relationship between changes in A_T (ΔA_T) and salinity (ΔS) in the upper 20 m is used following Eq. (5).

$$C_T = (\# \times S) + C_{TS=0} \quad (4)$$

$$A_T = (\# \times \Delta S) + \Delta A_{T\Delta S=0} \quad (5)$$

These values were added to the average C_T and A_T in the upper 20 m per year and used with CO2SYS with the average $Si(OH)_4$, PO_4, salinity, temperature and pressure to calculate a perturbed Ω. The change in Ω due to advective processes was estimated from the difference between the perturbed value and the 4-year average Ω. The effects of mixing on Ω ($\Delta\Omega_{mix}$) only account for the vertical flux of subsurface Atlantic Water with low-Ω (to differentiate mixing and advective processes) and were estimated from the inverse of the average mixed layer depth (MLD) during the observational year, the MLD anomaly ($MLD_{obs} - MLD_{ave}$) and the difference between average values of Ω for the Atlantic Water for each year per sub-region, adapted from Chierici et al. (2011). If $\Delta MLD < 0$, i.e. shallowing of the mixed layer in the observational year relative to the 4-year average, then the changes in Ω are assumed to be 0.

2.8. Uncertainties

The Ω anomalies determined using regional mean values in the upper 20 m in each observation year relative to the 4-year (2014–2017) average will include a degree of spatial variability due to the variable distribution of sampling stations. However, the temperature-salinity (and stable oxygen isotopic ratio of seawater) characteristics of the (upper) water column revealed that the inter-annual variability, as strongly controlled by sea ice cover, was much larger than the spatial variability in the physical–chemical characteristics. Therefore, the temporal variations in the reported variables are used to reveal key drivers of Ω anomalies. Uncertainties in the contributing components to ΔΩ were considered from errors associated with the input terms used in the anomaly calculations. Uncertainties were estimated from analytical precision as follows: $\Delta C_{T\ total}$ and $\Delta A_{T\ total}$ ± 2 μmol kg^{-1}; $\Delta C_{T\ temp}$ and $\Delta A_{T\ temp}$ were ±2 μmol kg^{-1}; $\Delta C_{T\ sal}$ and $\Delta A_{T\ sal}$ ± 2 μmol kg^{-1}; $\Delta C_{T\ adv}$ and $\Delta A_{T\ adv}$ were ±4 μmol kg^{-1}; $\Delta C_{T\ FW}$ and $\Delta A_{T\ FW}$ were ±2 μmol kg^{-1}. Uncertainties in $\Delta C_{T\ bio}$ and $\Delta A_{T\ bio}$ were estimated as ±1.5 μmol kg^{-1}from the analytical precision of NO_3 of ±3% and variability in the C:N ratio (±1 μmol kg^{-1}) to account for variations in the ratio from 6.6 (Redfield et al., 1963; Frigstad et al., 2014). The uncertainties in $\Delta A_{T\ CaCO3}$ and $\Delta C_{T\ CaCO3}$ were estimated as an upper bound of ±5 μmol kg^{-1} from the analytical precision of NO_3 (±3%) and A_T (±2 μmol kg^{-1}). Uncertainties in the calculated surface water pCO_2 (xCO_2) result from uncertainties in C_T, A_T, salinity, temperature, *K*1 and *K*2 that were added to each value of each property and used as inputs in CO2SYS to yield an upper bound error as ±10 μatm. Associated errors on $\Delta C_{T\ flux}$ are estimated as ±4 μmol kg^{-1}. A recent internal consistency study using CO_2 system data from 2015 in the Atlantic Water influenced Labrador Sea showed that the Mehrbach et al. (1973) constants yielded the closest agreement to measured values (Raimondi et al., 2019), but using A_T and C_T rather than A_T and pH (in 2015) likely overestimated pCO_2 by as much as 25 μatm. Therefore, the $pCO_2(A_T,C_T)$ values in 2014, 2016 and 2017 could be overestimated by an average of ~12 μatm. Therefore, the gradient relative to atmospheric CO_2 and CO_2 fluxes are likely to be greater, which would lead to a slight increase in $\Delta C_{T\ flux}$ and further decrease Ω in surface waters in 2014, 2016 and 2017.

3. Results

3.1. Hydrography and sea ice

The late summer (August-September) extent of sea ice exhibited large spatial variability during the study period (Fig. 3). Eastern Fram Strait and Hinlopen Strait typically had low sea ice cover each year and the shelf region displayed some variability in sea ice conditions. The MIZ had higher sea ice cover relative to the other three sub-regions with large inter-annual variability in the southward extent of the ice edge. The largest extent of summer sea ice, from Fram Strait to the northern Barents Sea, occurred during 2014 and the ice edge north of Svalbard was located at ~80°N. In contrast, 2015 had much reduced sea ice cover by late summer and, as such, the transect from Hinlopen Strait across the northern shelf was extended farther north into the seasonal pack ice of the Nansen Basin. The ice edge north of Svalbard was at ~81°N, around 110 km farther north than during 2014. The years 2016 and 2017 were initially characterised by similar ice conditions to those in 2014,

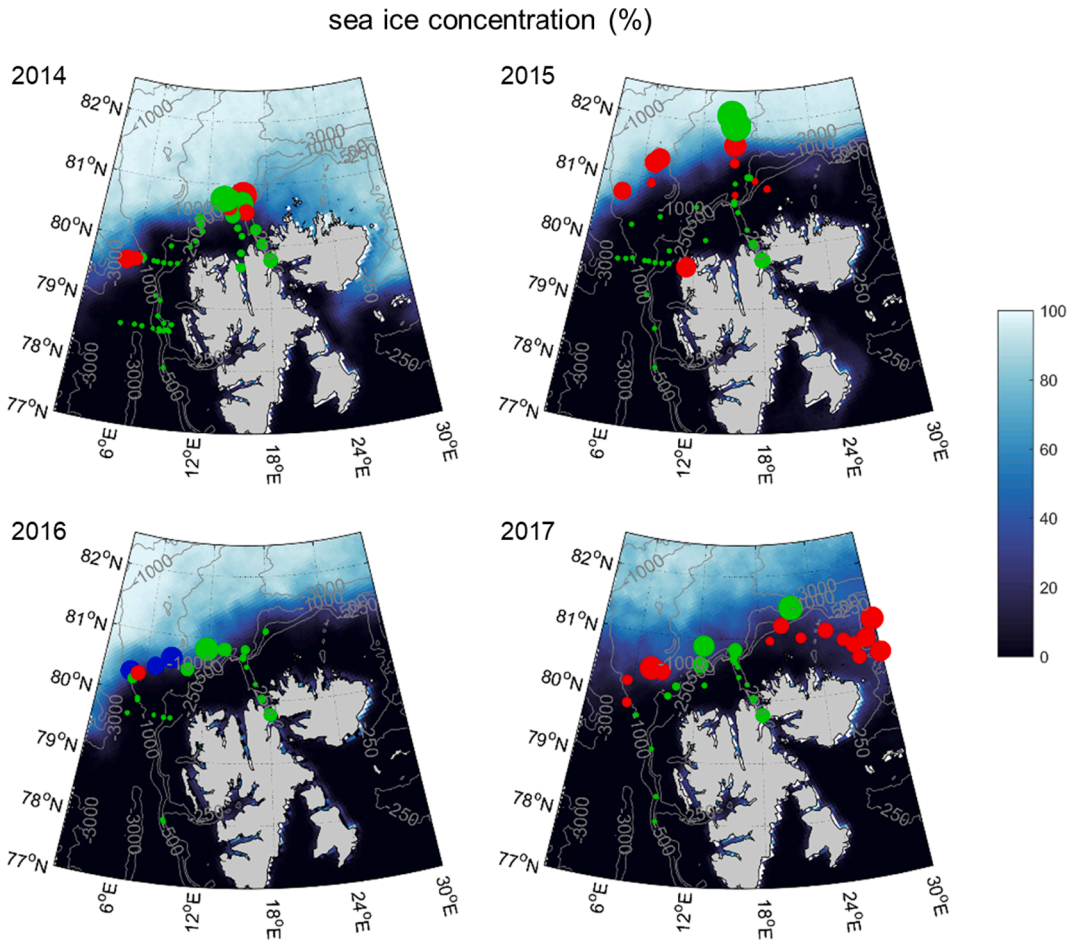

Fig. 3. The background ice map shows the average ice concentration in August and September for each study year (2014–2017). The colored circles show the station locations. Circle size indicates the sea ice concentration in the last 30 days (average from daily sea ice concentration data from the Advanced Microwave Scanning Radiometer 2). Circle color indicates the sea ice concentration trend in the last 30 days (linear trend in ice concentration in the last 30 days, if the r^2 was < 0.2 the trend was set to 0): Green – no trend, blue – increase and red – decrease. Isobaths were derived from the International Bathymetric Chart of the Arctic Ocean (IBCAO) bathymetry and the Matlab toolbox m_map was used for mapping. (For interpretation of the references to color in this figure legend, the reader is referred to the web version of this article.)

however rapid retreat occurred with the ice edge generally following the shelf-break north of Svalbard at ~80.5°N.

Spatially, surface waters were warmest (6–9 °C) and most saline (34.8–35.1) along the Atlantic Water inflow from eastern Fram Strait and the north-western shelf (Fig. 4). Sea surface temperatures were lowest (<0 °C) in the MIZ from the western flank of the Yermak Plateau to the seasonal ice pack at 82°N (in 2015), and to the shelf break north of Svalbard and across the shelf northeast of Nordaustlandet (in 2017). Relatively fresh surface waters ($S \sim 32$) were consistently found in the MIZ. Lower $\delta^{18}O$ values (<1‰) were characteristic of surface waters in Hinlopen Strait and the northern shelf. In 2015, average surface temperatures were generally higher compared with the other years. This was accompanied by higher $\delta^{18}O$ values of 0.45 ± 0.24‰. In contrast, surface waters in 2017 had lower salinity and reduced temperatures and lower $\delta^{18}O$ between −0.02‰ and −0.73‰ as an indication of increased meteoric water fraction mixed into the background of Atlantic Water.

The surface layer (mixed layer, average depth 21 m) and upper water column was characterised by fresher and often colder waters (Fig. 5a-b) of PSW and PSWw (Fig. 2). The values of $\delta^{18}O$ and salinity increased rapidly below the surface layer up to about 50 m depth and become more uniform at about 0.3–1‰ and 34.9, respectively (Fig. 5b-c). Lower $\delta^{18}O$ values (typically < 0.50‰) were a signal of meteoric water (glacial meltwater, river runoff, snow melt, rain) mixing with sea-ice melt and surface seawater. Higher $\delta^{18}O$ values up to ~1‰ in Atlantic Water were indicative of oceanic-sourced waters (Table 1). Subsurface waters were dominated by Atlantic Water from 600 to 700 m depth up to the surface layer (Fig. 2), which showed the largest inter-annual variability in water mass characteristics (Fig. 5). Below 1000 m depth in the Nansen Basin, AIW could de distinguished by potential temperatures<0 °C (Figs. 5-6) and $\delta^{18}O$ values of 0.46 ± 0.14‰ (Fig. 5c; Table 1). In 2015, the distribution of $\delta^{18}O$ with respect to salinity shows that the water column was typically isotopically enriched with greater volume and/or influence of Atlantic Water across the region (Fig. 5c). Colder water with higher $\delta^{18}O$ values occurred in the northern extent in the MIZ in 2015. In 2017, a colder halocline and lower temperatures were found over the shelf and northeast of Nordaustlandet. This indicates that significant cooling of the water column took place, which coupled to lower $\delta^{18}O$, is likely linked to late retreat of the ice pack and influx of snow and sea-ice meltwater and subsequent mixing with surface waters.

3.2. Carbonate chemistry and ocean acidification state

Surface water C_T and A_T were highest in eastern Fram Strait and along the northern and western shelf and were low in the MIZ throughout the 4-year study period (Fig. 7). The distribution of C_T and A_T in the full water column showed that the lowest values occurred in the fresh PSW and PSWw layers (Fig. 5d-e; Table 1). Values generally increased with depth to the highest C_T in AIW and highest A_T occurred in Atlantic Water. Inter-annual variability was found in the upper 500 m (Fig. 5d-e). Highest average surface water C_T and A_T of ~2006 μmol

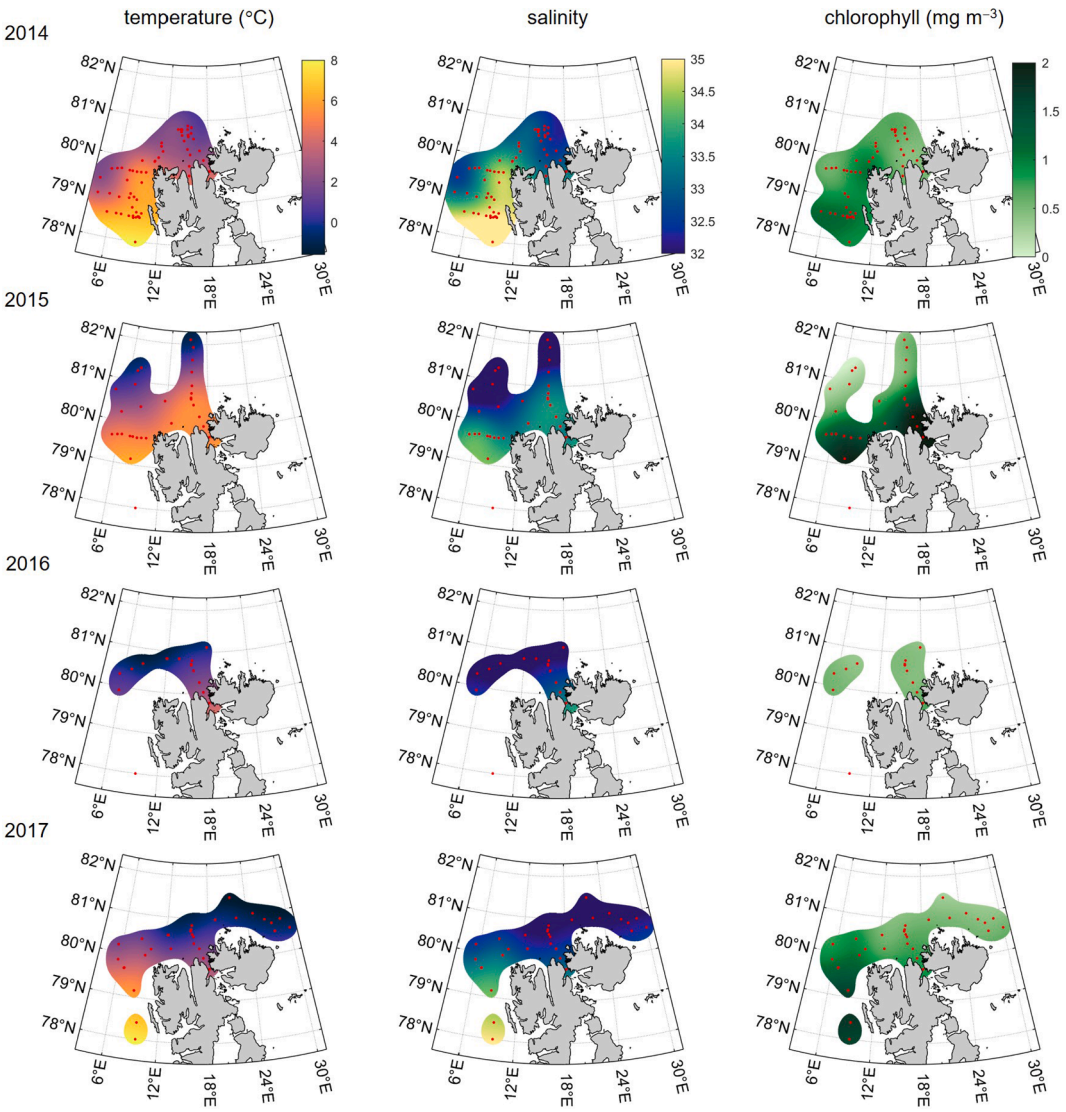

Fig. 4. Surface water temperature (°C), practical salinity and chlorophyll (mg m^{-3}) across the region in 2014, 2015, 2016 and 2017. The Matlab toolbox m_map was used for mapping.

kg^{-1} and ~2215 μmol kg^{-1}, respectively, occurred in 2015 (Fig. 7). Conversely, the lowest average sea surface C_T and A_T of ~1962 μmol kg^{-1} and ~2157 μmol kg^{-1}, respectively, occurred in 2016. Relative to the 4-year average (Table 1), Atlantic Water had higher C_T (~2165 μmol kg^{-1}) and A_T (~2320 μmol kg^{-1}) in 2015 and lower A_T (~2313 μmol kg^{-1}) in 2016 and 2017, which also includes large spatial variability in each sub-region.

The variability of Ω in the water column showed highest values (Ω > 2) in the PSW and PSWw (Fig. 6) and a saturated water column (Fig. 5f) (Ω > 1) in the upper 2000 m. Surface water Ω ranged between 1.87 and 2.65 with higher values occurring in eastern Fram Strait and the northern shelf and lower values in the MIZ (Fig. 8). Values decreased with depth to ~1.68 in Atlantic Water and ~1.20 in AIW (Table 1). Compared with the other regions, AIW in the MIZ was found deeper and over a wider range from 700 m to 2630 m and had more variable Ω of 1.16 ± 0.10. The saturation horizon (Ω = 1) was located within the depth range 1800–2240 m in the Nansen Basin and near-saturation of aragonite 0.98 was found at the discrete depths of 2237, 2410 and 2431 m at 81.3–82.1°N, 15.2–15.5°E in the MIZ. Inter-annual variability in Ω in the upper 500 m (Fig. 5f) showed that surface waters in 2015 had higher Ω of ~2.26 compared with lower average values of ~2.05 in 2016 (Fig. 8). Relative to the 4-year average (Table 1), Ω in Atlantic Water varied from ~1.78 in 2014 to ~1.65 in 2016 and 2017.

3.3. *Air-sea CO_2 fluxes*

Surface waters were strongly undersaturated with pCO_2 142–302 μatm with respect to atmospheric CO_2 (pCO_2 range 380–389 ± 1 μatm) across all regions and all years (Fig. 8). Warmer waters of eastern Fram Strait generally had the least undersaturation (ΔpCO_2 ~ −90 μatm) and strongest CO_2 undersaturation (ΔpCO_2 ~ −240 μatm) occurred in the MIZ and ice-influenced waters over the shelf. Atmospheric CO_2 sink potential in the MIZ was greatest out of all regions and the air-sea CO_2 flux varied between −28.9 mmol m^{-2} day^{-1} in 2014 and −9.3 mmol m^{-2} day^{-1} in 2016. However, these potentially strong CO_2 sinks were dampened by 48–89% sea ice cover (Figs. 2 and 8).

In 2014, regional ΔpCO_2 was on average −169 μatm and, combined with higher monthly wind speeds, created the strongest regionally averaged CO_2 fluxes of −20.4 mmol m^{-2} day^{-1}, i.e. substantial CO_2 sinks, out of the 4-year study period (Table 2). Due to the greater extent sea ice in 2014, ice-scaled CO_2 fluxes were reduced the most by ~35% to an average of −13.3 mmol m^{-2} day^{-1} (Fig. 8). In 2015, surface waters were least CO_2-undersaturated with average ΔpCO_2 of about −158 μatm and associated fluxes and ice scaled fluxes were −12.6 and −9.5 mmol

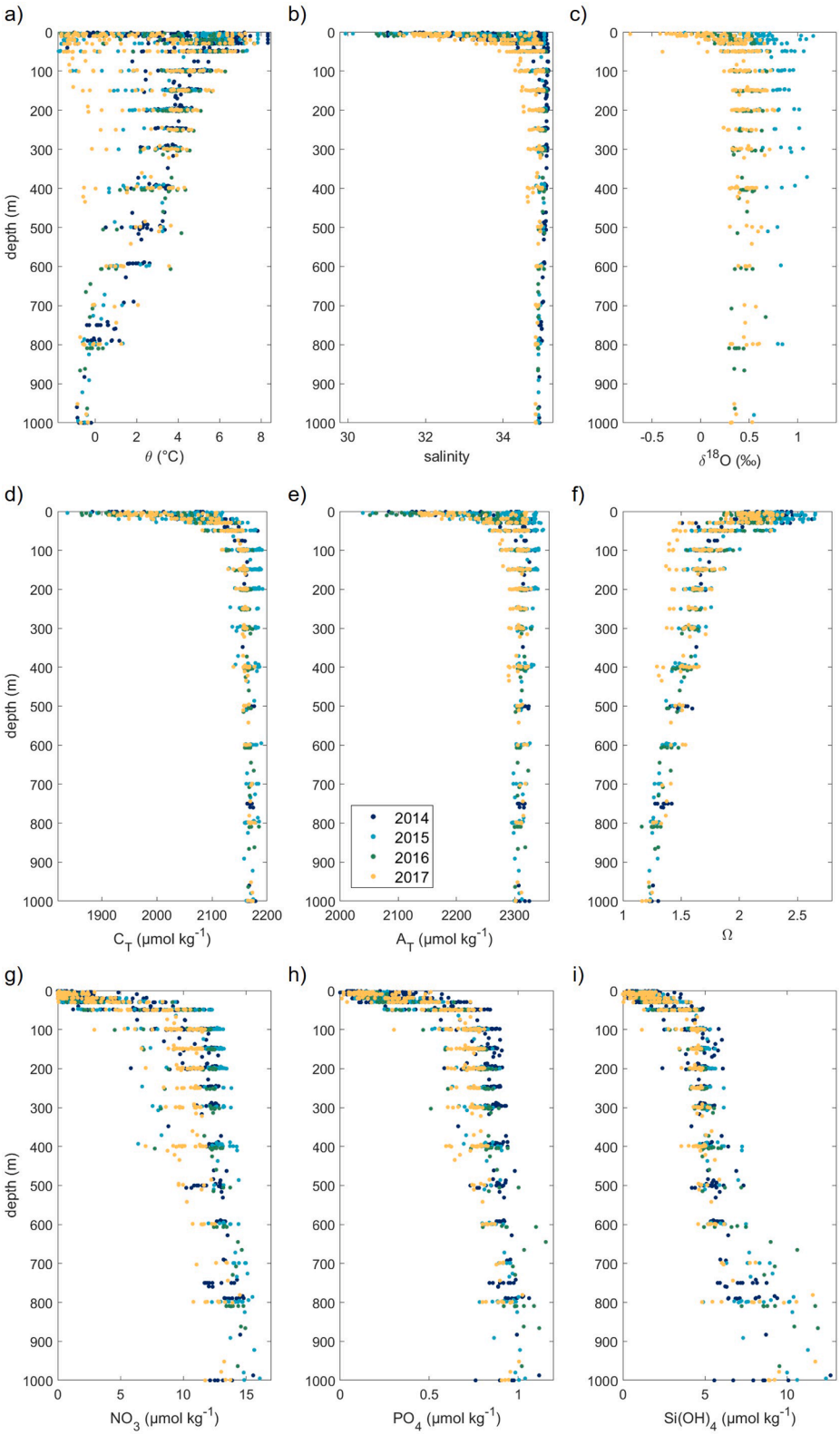

Fig. 5. Profiles of (a) potential temperature (θ, °C), (b) practical salinity, (c) stable oxygen isotopic ratio ($\delta^{18}O$;‰), (d) C_T (μmol kg^{-1}), (e) A_T (μmol kg^{-1}), (f) Ω, (g) NO_3 (μmol kg^{-1}), (h) PO_4 (μmol kg^{-1}), (i) $Si(OH)_4$ (μmol kg^{-1}) in the upper 1000 m of the water column during late summer in 2014 (dark blue dots), 2015 (light blue dots), 2016 (green dots) and 2017 (yellow dots) in all sub-regions. (For interpretation of the references to color in this figure legend, the reader is referred to the web version of this article.)

m^{-2} day^{-1}, respectively. In 2016, ΔpCO_2 was on average −179 μatm and weakest monthly wind speeds yielded the lowest oceanic uptake of atmospheric CO_2 with a flux of −11.1 mmol m^{-2} day^{-1}. Fluxes were reduced by ~22% to an average of −8.6 mmol m^{-2} day^{-1} due to ice cover. Greatest sea surface CO_2 undersaturation in 2017 yielded average ΔpCO_2 of −180 μatm and fluxes of −15.0 mmol m^{-2} day^{-1}. Accounting for sea ice cover, air-sea CO_2 fluxes were reduced to an average of −11.5 mmol m^{-2} day^{-1}. The regionally-averaged supply of C_T to the mixed layer ($\Delta C_{T\ flux}$) as a result of atmospheric CO_2 drawdown varied from highest ~21 μmol kg^{-1} $month^{-1}$ in 2014 to lowest ~12 ± 4 μmol kg^{-1} $month^{-1}$ in 2016 (Table 2).

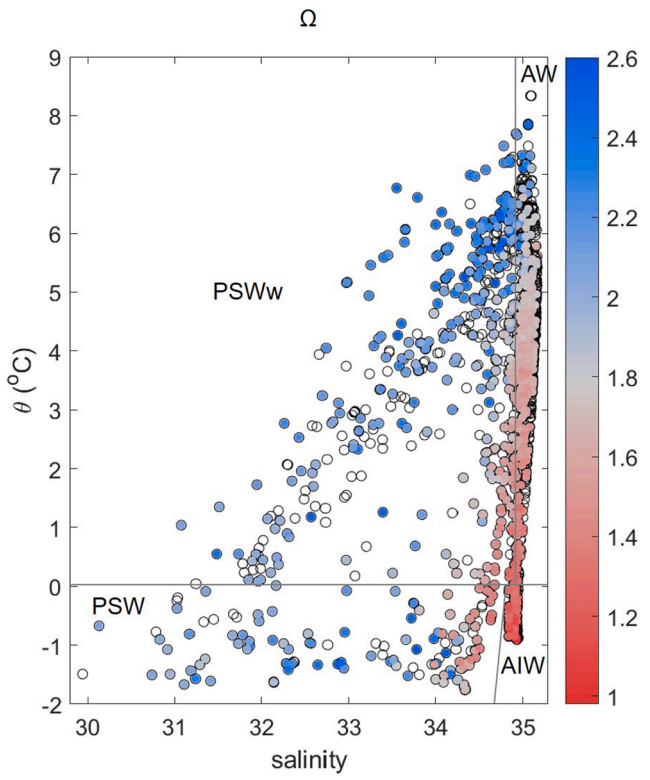

Fig. 6. Potential temperature (θ, °C) plotted against practical salinity for all SI-ARCTIC and CarbonBridge CTD stations 2014–2017 (black open circles) and for those with ocean acidification variables (shaded based on Ω values) delineating Polar Surface Water (PSW), warm Polar Surface Water (PSWw), Atlantic Water (AW) and Arctic Intermediate Water (AIW) following Rudels et al. (2005) and Pérez-Hernández et al. (2017).

3.4. Inorganic nutrients

Water column concentrations of nitrate (NO_3), phosphate (PO_4) and silicate ($Si(OH)_4$) ranged from 0–16.3 μmol kg^{-1}, 0–1.16 μmol kg^{-1} and 0–13.3 μmol kg^{-1}, respectively (Fig. 5g-i). Lowest concentrations of all macronutrients were found in the PSW and PSWw (Table 1) and depleted NO_3 occurred in surface waters in all sub-regions. Concentrations of all macronutrients typically increased with depth to the Atlantic Water (Fig. 5g-i). Highest NO_3 (15–16 μmol kg^{-1}) and $Si(OH)_4$ (12–13 μmol kg^{-1}) characterised the AIW. Inter-annual variability all macronutrients occurred in the upper 500 m. Relative to the 4-year average, Atlantic Water had lower $Si(OH)_4$ (4.12 ± 1.48 μmol kg^{-1}) and NO_3 (9.23 ± 4.29 μmol kg^{-1}) in 2014 (n = 541) and conversely higher $Si(OH)_4$ (4.98 ± 1.11 μmol kg^{-1}) and NO_3 (11.55 ± 2.82 μmol kg^{-1}) in 2015 (n = 168). In 2014 and 2015, elevated concentrations of NO_3 and $Si(OH)_4$ were found in the AIW. In 2014, PO_4 was higher between 100 m and 500 m.

3.5. Chlorophyll

In 2014, average sea surface chlorophyll concentrations were 0.78 ± 0.43 mg m^{-3} (n = 46) with highest concentrations up to 1.73 mg m^{-3} in eastern Fram Strait (Fig. 4). In 2015, surface water chlorophyll was highest relative to the other years, with average concentrations of 1.14 ± 0.99 mg m^{-3} (n = 27) and maximum values up to 4.03 mg m^{-3} in the MIZ. Surface waters in 2016 and 2017 had lower concentrations relative to the 4-year study period, with lowest regionally averaged values of 0.51 ± 0.29 mg m^{-3} (n = 13) in 2016. The reduced chlorophyll across the shelf regions in 2014, 2016 and 2017 is likely associated with the timing of the sea ice retreat that happened later due to the greater sea ice cover (2014) and rapid transition from ice-covered waters during early August to recently exposed surface water by early September (2016 and 2017).

3.6. Physical-chemical coupling and biogeochemical cycling

Values of $\delta^{18}O$ exhibited variability relative to salinity, particularly in the surface layer (Fig. 9a), however average $\delta^{18}O$ in the key water masses had little difference (0.28–0.55‰; Table 1) as a result of the dominant oceanic $\delta^{18}O$ signal. Water column $\delta^{18}O$ was comparatively higher and lower in 2015 and 2017, respectively. In the surface layer, negative $\delta^{18}O$ values predominantly occurred in PSW and indicate a stronger influence of meteoric water (glacial meltwater, precipitation, river runoff, rain). Positive $\delta^{18}O$ values occurred in PSWw and indicate that sea-ice meltwater is the predominant freshwater source. Lower $\delta^{18}O$ reported in sea ice, and subsequently in sea ice meltwater, can also occur due to snow meltwater percolating the ice pack and localised riverine influence (Fransson et al., 2020). The $\delta^{18}O$ signature of freshwater was estimated as −2.00 ± 0.73‰ (r^2 = 0.10, p < 0.01, n = 104) from the salinity-$\delta^{18}O$ relationship in the mixed layer. This value is a composite of the regional values of $\delta^{18}O_{S=0}$ that varied from −5.59‰ in Hinlopen Strait to −0.88‰ in the MIZ (Table 4). Across all regions, A_T and C_T closely followed the variations in salinity (Fig. 9b). The correlation between A_T and salinity in the upper 20 m yielded $A_T = 60.6S + 205$ (r^2 = 0.93, se = 35 μmol kg^{-1}, p < 0.01, n = 240). The correlation between C_T and salinity in the upper 20 m yielded $C_T = 55.76S + 160$ (r^2 = 0.84, se = 52 μmol kg^{-1}, p < 0.01, n = 238). These relationships reveal evidence of freshwater endmembers for A_T and C_T with regionally-averaged values of 205 ± 35 μmol kg^{-1} and 160 ± 52 μmol kg^{-1}, respectively; composite values of the A_T and C_T freshwater endmembers estimated per sub-region (Table 4).

The relationships of [CO_3^{2-}], Ω, pH_T and pCO_2 show variable patterns across a range of salinities in the different water masses (Fig. 9c-f). At lower salinities, the variables become more decoupled. Highest [CO_3^{2-}] of ~175 μmol kg^{-1} and maximum Ω of 2.65 were found in the warmer surface layer of PSWw. Highest pH_T (8.42) and lowest pCO_2 of ~140 μatm (most undersaturated with respect to atmospheric CO_2) were concurrent with lowest C_T and A_T in the fresh, colder PSW. Higher pCO_2 (400–430 μatm) and generally lower pH_T (8.01–8.21) occurred with highest C_T and A_T in the warm and saline Atlantic Water. Lowest [CO_3^{2-}] of ~91 μmol kg^{-1} and, through chemical proportionality, lowest Ω of ~1 were concurrent with pH_T around 8.01 in the C_T-rich and colder, fresher AIW. Inter-annual variability can be seen in the upper layers where surface water [CO_3^{2-}], Ω and pH_T were generally higher in 2014 and 2015 and lower in 2016. In 2015, surface waters were characterised by highest $\delta^{18}O$, [CO_3^{2-}], Ω, pH_T and lowest pCO_2 relative to the other years.

All water column data yielded nutrient uptake ratios for C:N of 11.3 ± 0.3, N:P of 17.5 ± 0.1 and Si:N of 0.4 ± 0.0 by late summer (Fig. 10; Table 5). Some interesting features with significant relationships can be identified: (i) relative to the whole water column, mixed layer C:N was elevated at 31.0 ± 3.3 and N:P was lower at 10.0 ± 0.3 ; (ii) Atlantic Water ratios of C:N were much lower at 5.3 ± 0.2 and N:P was higher at 18.8 ± 0.2 compared with mixed layer ratios; (iii) the Si:N ratio in AIW was higher at 1.4 ± 0.1 relative to the whole water column. Inter-annual variability in the nutrient ratios showed higher N:P ratios, driven by relatively high NO_3 concentrations with respect to PO_4, in 2015 (Fig. 10a). Lower Si:N uptake ratios in 2014 reflect reduced biological production in the colder, ice-covered waters (Fig. 10b). Higher C:N uptake ratios in 2014 and 2017 resulted from a comparatively C_T-rich water column (Fig. 10c). Uptake ratios of Si:N were elevated at higher concentrations and relatively silicate-rich AIW in 2017. These reveal different stoichiometry between water masses and deviations from the Redfield ratio (Redfield et al, 1963). Highest chlorophyll concentrations (>3 mg m^{-3}) were frequently associated with near-depleted NO_3 in the mixed layer (Fig. 10d).

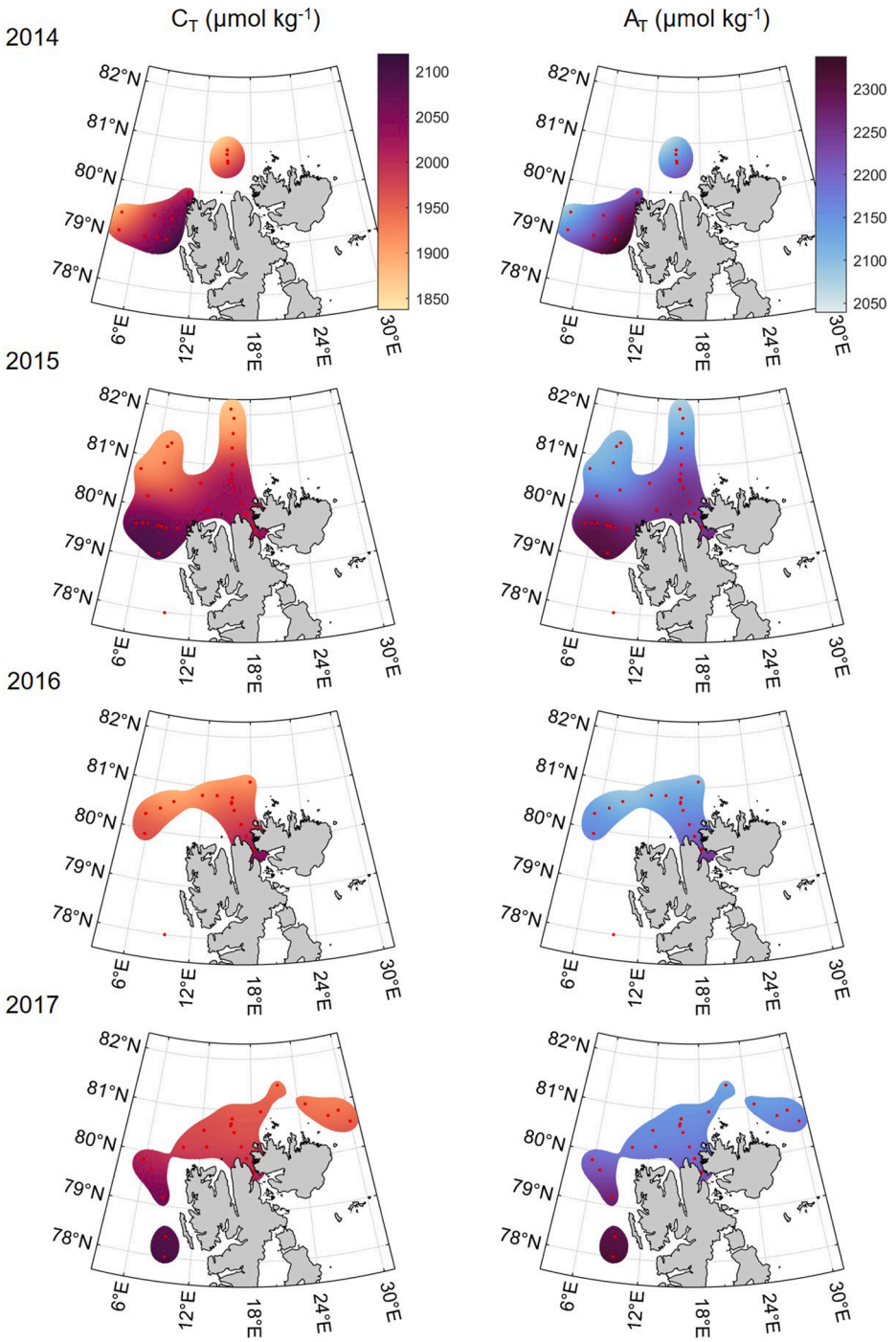

Fig. 7. Surface water C_T (µmol kg^{-1}) and A_T (µmol kg^{-1}) across the region in 2014, 2015, 2016 and 2017. The Matlab toolbox m_map was used for mapping.

3.7. Major controls on regional ocean acidification states

The inter-annual variability in mixed layer Ω during late summers 2014 to 2017 is driven by physical and biogeochemical processes, which are intrinsically linked to the meteorological, oceanographic and sea ice conditions, that generated Ω anomalies each year relative to the 4-year average. Despite the spatial variability in year-to-year sampling within each subregion (except for Hinlopen Strait), distinct regional traits in Ω and inter-annual variability in ΔΩ anomalies could be identified. During the 4-year study period, biological production/respiration, formation/dissolution of biotic and abiotic calcium carbonate minerals (aragonite, calcite, ikaite), mixing and advection of water masses dominated the variability in Ω (Fig. 11). Air-sea CO_2 exchange and the influence of freshwater containing A_T and C_T also played important roles. Effects of changes in salinity and temperature were minor.

From a regional perspective, eastern Fram Strait and the MIZ displayed the greatest and smallest range in ΔΩ anomalies, respectively (Fig. 11a). Eastern Fram Strait is strongly influenced by Atlantic Water inflow and varying sea ice cover and the MIZ had consistent ice cover, although a wider regional extent. The northern shelf and Hinlopen Strait exhibited similar patterns in the ΔΩ anomalies, both being Svalbard shelf systems along the Atlantic Water inflow pathway. Key controls of ΔΩ, as determined from the largest inter-annual ranges (Fig. 11a) and greatest relative proportions (Fig. 11b), were $\Delta\Omega_{CaCO3}$ (−0.05 to 0.03; up to 62% of the total ΔΩ) over the northern shelf; $\Delta\Omega_{CaCO3}$ (−0.12 to 0.06; up to 52% of the total ΔΩ) in eastern Fram Strait; $\Delta\Omega_{bio}$ (−0.05 to

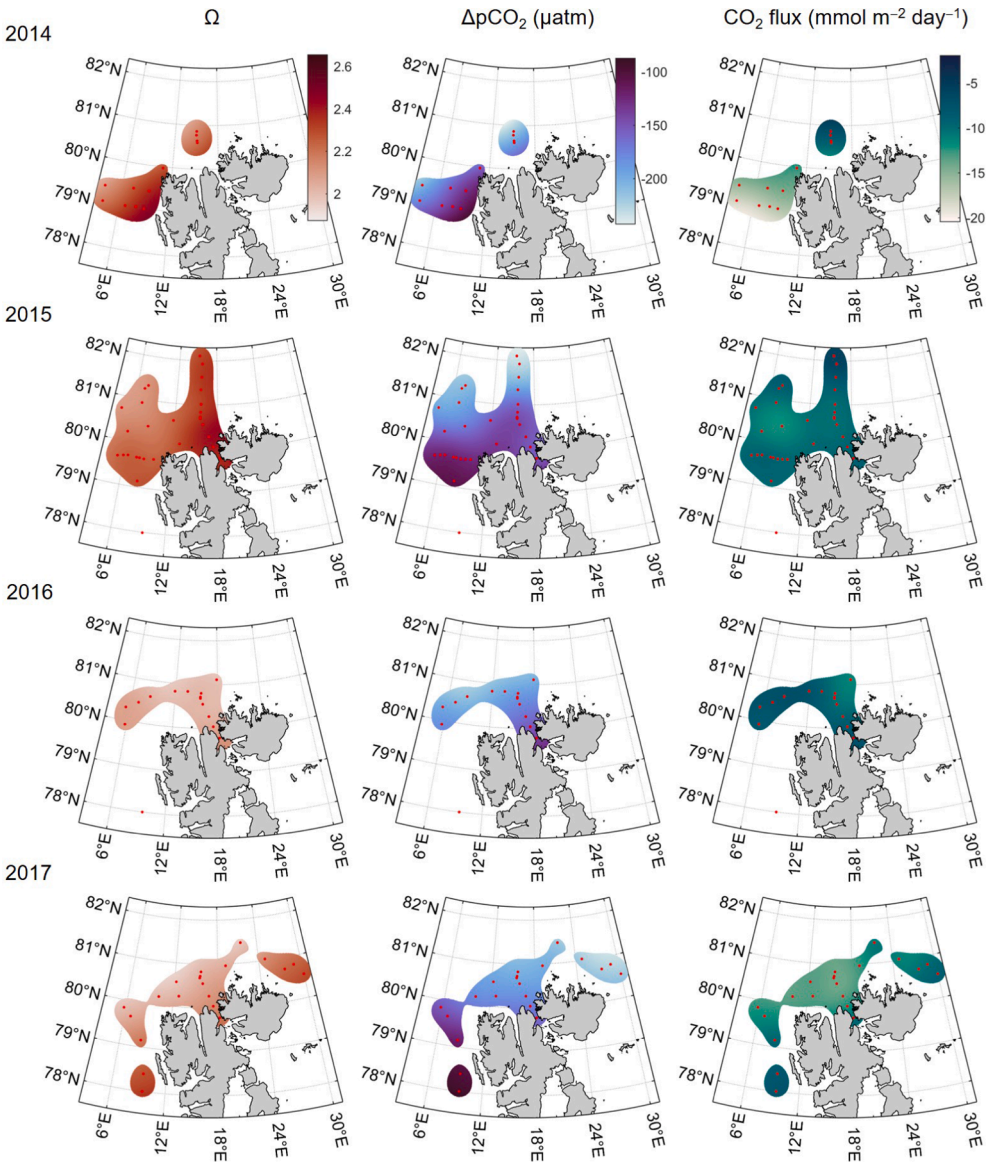

Fig. 8. Surface water Ω, ΔpCO_2 (μatm) and sea-ice scaled air-sea CO_2 flux (mmol m^{-2} day^{-1}) across the region in 2014, 2015, 2016 and 2017. The Matlab toolbox m_map was used for mapping.

0.06; up to 45% of the total ΔΩ) in Hinlopen Strait; $\Delta\Omega_{bio}$ (−0.03 to 0.03; up to 35% of the total ΔΩ) in the MIZ.

In 2014, photosynthesis/respiration was the key driver of Ω anomalies, representing 1–45% of the total ΔΩ with $\Delta\Omega_{bio}$ ranging between 0 and −0.05 as a result of anonymously low biological production relative to the other years. In 2015, photosynthesis/respiration and $CaCO_3$ processes were important with positive $\Delta\Omega_{bio}$ of 0.01–0.06 (7–45% of the total ΔΩ) in response to higher primary production and $\Delta\Omega_{CaCO3}$ ranging between −0.04 and 0.06 (13–52% of the total ΔΩ) due to anonymously low and high $CaCO_3$ dissolution, respectively. Advection was also important as $\Delta\Omega_{adv}$ ranged between −0.02 and 0.06 (9–27% of the total ΔΩ) as a result of mixing of waters with lower (fresher Arctic) and higher (saline Atlantic) Ω values, respectively. Anomalies in 2016 were driven reduced $CaCO_3$ dissolution with $\Delta\Omega_{CaCO3}$ ranging between −0.12 and 0.01, representing 13–34% of the total ΔΩ. In 2017, vertical mixing dominated the inter-annual variability and accounted for 27–58% of the total ΔΩ with $\Delta\Omega_{mix}$ from −0.15 to −0.04 due to the instantaneous imprint of low-Ω Atlantic Water into the mixed layer.

4. Discussion

4.1. Ice-covered Arctic regime and increased surface water acidification

The sea ice conditions during the 4-year study period displayed inter-annual variability that reflects the coupled ice-ocean system of the Atlantic Water inflow region (Ivanov et al., 2018). The greatest extent of summer sea ice in 2014 and more southerly ice edge at ~80°N resulted in a reduced amount of light incident on surface waters, thus limiting the length of the growing season. This resulted in strong negative $\Delta\Omega_{bio}$ (−0.05 to −0.01) as a result of anomalously low biological production in the Arctic-like conditions across the region in 2014. The occurrence of non-depleted macronutrients and higher C:N uptake ratios, accompanied by lower chlorophyll concentrations (<1 mg m^{-3}), indicated that phytoplankton production and biological CO_2 fixation were in an early phase in 2014. The delayed progression in primary production and comparatively high C_T (~2009 μmol kg^{-1}) in the surface layer lessened the extent of biologically-enhanced Ω by late summer. This emphasises the importance of sea ice retreat and meltwater-driven stratification for summer carbon and nitrate drawdown in this region (Leu et al., 2011;

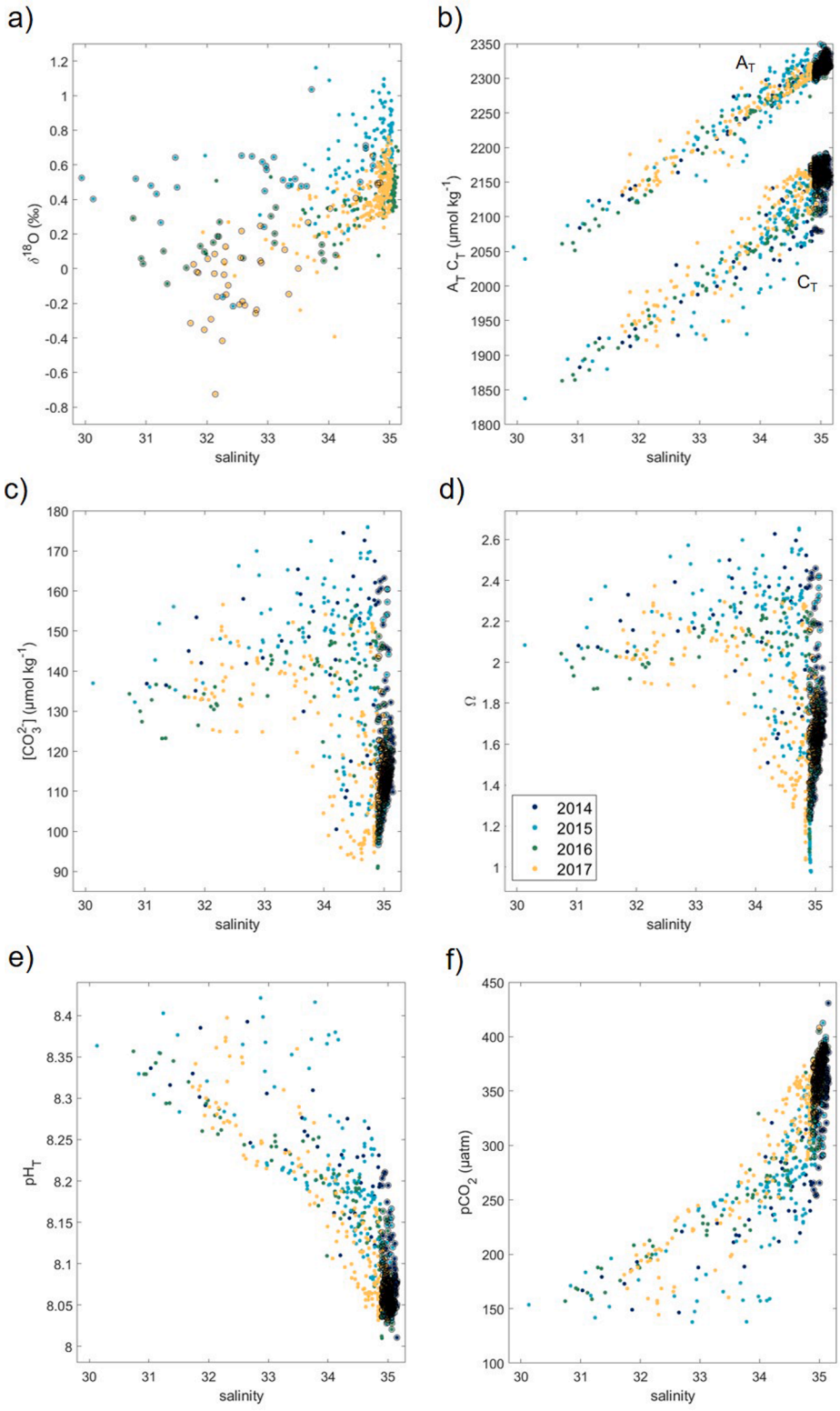

Fig. 9. Relationships between practical salinity and (a) $\delta^{18}O$ (‰) with surface layer samples highlighted (black open circles), (b) A_T (μmol kg^{-1}) and C_T, (c) $[CO_3^{2-}]$, (d) Ω, (e) pH_T, (f) pCO_2 during late summer in 2014 (dark blue dots), 2015 (light blue dots), 2016 (green dots) and 2017 (yellow dots) in all subregions. Atlantic Water is highlighted (black open circles) in (b)-(f). (For interpretation of the references to color in this figure legend, the reader is referred to the web version of this article.)

Randelhoff et al., 2018; Henley et al., 2020).

Extensive sea ice cover likely restricted widespread wind-driven mixing and subsequently reduced nutrient replenishment from underlying Atlantic Water. South of the ice edge, surface waters along the inflow shelves were relatively warm (θ ~ 2.9 °C) and saline (S ~ 33.0) and exhibited a greater proportion of PSWw (relative to PSW) and an absence of significant meltwater effects. The subsurface Atlantic Water mixed into the weakly stratified mixed layer and elevated A_T (~2226 μmol kg^{-1}), relative to C_T, resulting in increased buffering capacity. Therefore, ice-free surface waters had higher $[CO_3^{2-}]$ of ~151 μmol kg^{-1} and Ω of ~2.28, relative to the 4-year average for PSWw. Negative $\Delta\Omega_{CaCO3}$ anomalies as low as −0.05 were prevalent across the whole region (except for Hinlopen Strait) in 2014. This signal of less $CaCO_3$ dissolution resulted in anomalously low $[CO_3^{2-}]$ that acted to lower

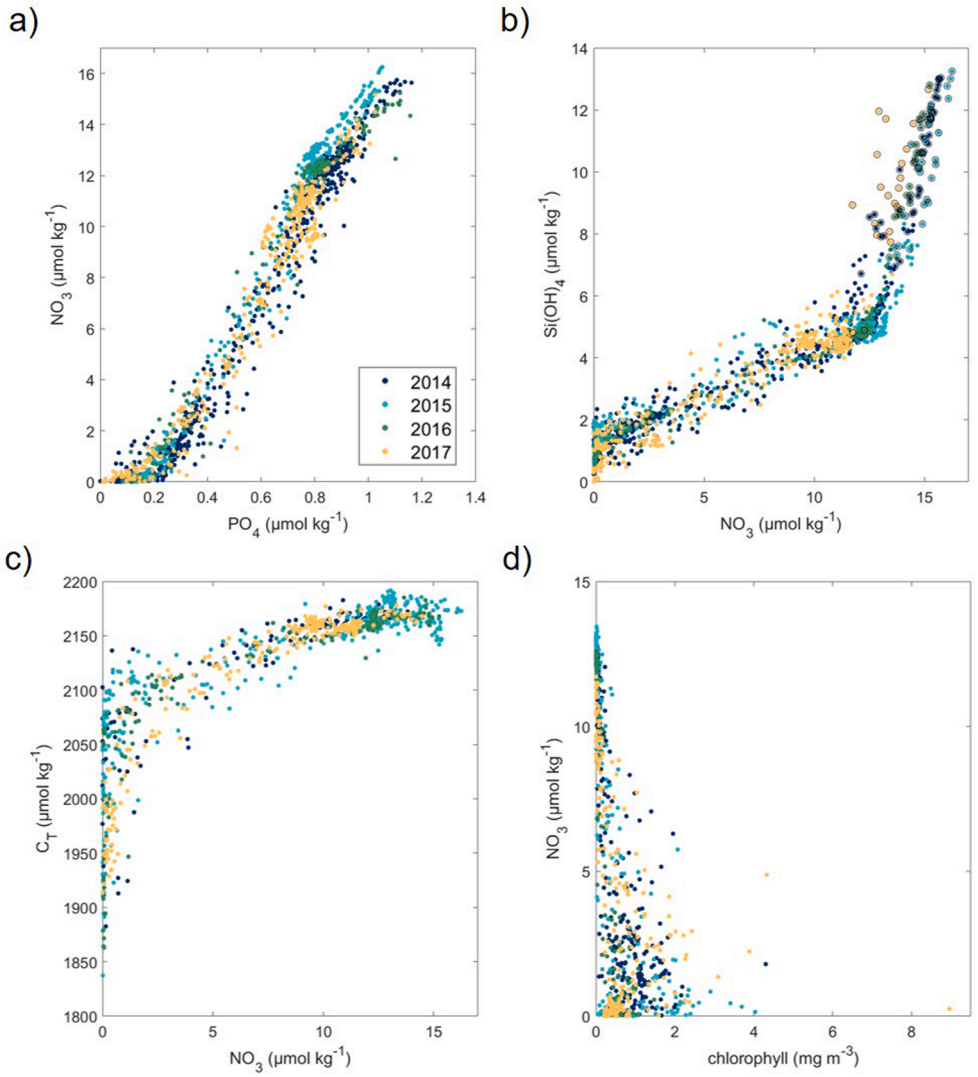

Fig. 10. Relationships between (a) NO_3 (µmol kg^{-1}) and PO_4 (µmol kg^{-1}), (b) $Si(OH)_4$ (µmol kg^{-1}) and NO_3 (µmol kg^{-1}), (c) C_T (µmol kg^{-1}) and NO_3 (µmol kg^{-1}), (d) NO_3 (µmol kg^{-1}) and chlorophyll (mg m^{-3}), during late summer in 2014 (dark blue dots), 2015 (light blue dots), 2016 (green dots) and 2017 (yellow dots) in all sub-regions. (For interpretation of the references to color in this figure legend, the reader is referred to the web version of this article.)

Table 5
Linear regression relationships for (1) nutrient uptake ratios between inorganic carbon (C), nitrate (N), phosphate (P) and silicate (Si) in the full water column, mixed layer and key water masses and (2) aragonite saturation state (Ω) and freshwater fraction (FW) in the surface layer. Regression analysis information: gradient ± standard error (se), r^2, p value and n number of observations for statistically significant relationships.

Linear regression relationship	Gradient ± se	r^2	p	n
C/N	11.3 ± 0.3	0.70	≪0.01	873
C/N mixed layer	31.0 ± 3.3	0.28	≪0.01	226
C/N Atlantic Water	5.3 ± 0.2	0.73	≪0.01	402
N/P	17.5 ± 0.1	0.96	0.00	1462
N/P mixed layer	10.0 ± 0.3	0.73	≪0.01	394
N/P Atlantic Water	18.8 ± 0.2	0.94	0.00	113
Si/N	0.41 ± 0.0	0.75	0.00	1471
Si/N Arctic Intermediate Water	1.4 ± 0.1	0.59	≪0.01	113
Ω/FW surface layer 2014	−0.028 ± 0.006	0.71	<0.01	12
Ω/FW surface layer 2015	−0.016 ± 0.005	0.25	<0.01	30
Ω/FW surface layer 2016	−0.025 ± 0.006	0.56	<0.01	16
Ω/FW surface layer 2017	−0.026 ± 0.008	0.34	<0.01	22

surface water Ω. This was particularly evident in eastern Fram Strait and over the northern shelf. This could result from less $CaCO_3$ dissolution from in situ and/or advected shells and skeletons of pelagic calcifiers (Chierici et al., 2019), which constitute a geochemical buffer and are discussed further in section 4.3. Less meltwater influence and subsequent reduction in ice-derived $CaCO_3$ (ikaite) is likely to play a minor role, discussed further in Section 4.4.

Surface waters in 2014 had greatest potential for oceanic uptake of atmospheric CO_2 with average fluxes of −20.4 ± 5.9 mmol m^{-2} day^{-1}, driven by lower C_T in the wider expanse of cold and fresh ice-influenced waters. Although chlorophyll concentrations were not as high as those reported during the spring bloom in the area (Randelhoff et al., 2018), likely CO_2 drawdown from both under-ice blooms by the haptophyte algae *Phaeocystis pouchetii* (Assmy et al., 2017) and in open water was evident from near-depleted nitrate and reductions in C_T. However, the larger areal extent of summer sea ice cover is expected to have inhibited air-sea CO_2 exchange, depending on the number of cracks, leads and degree of permeability of decaying sea ice (Loose et al., 2009; Fransson et al., 2017). As such, drawdown of atmospheric CO_2 predominantly occurred in the surface waters that were recently exposed and predominantly ice-free, e.g., eastern Fram Strait. Despite similar ranges in the degree of CO_2 undersaturation in seawater (ΔpCO_2 between −243

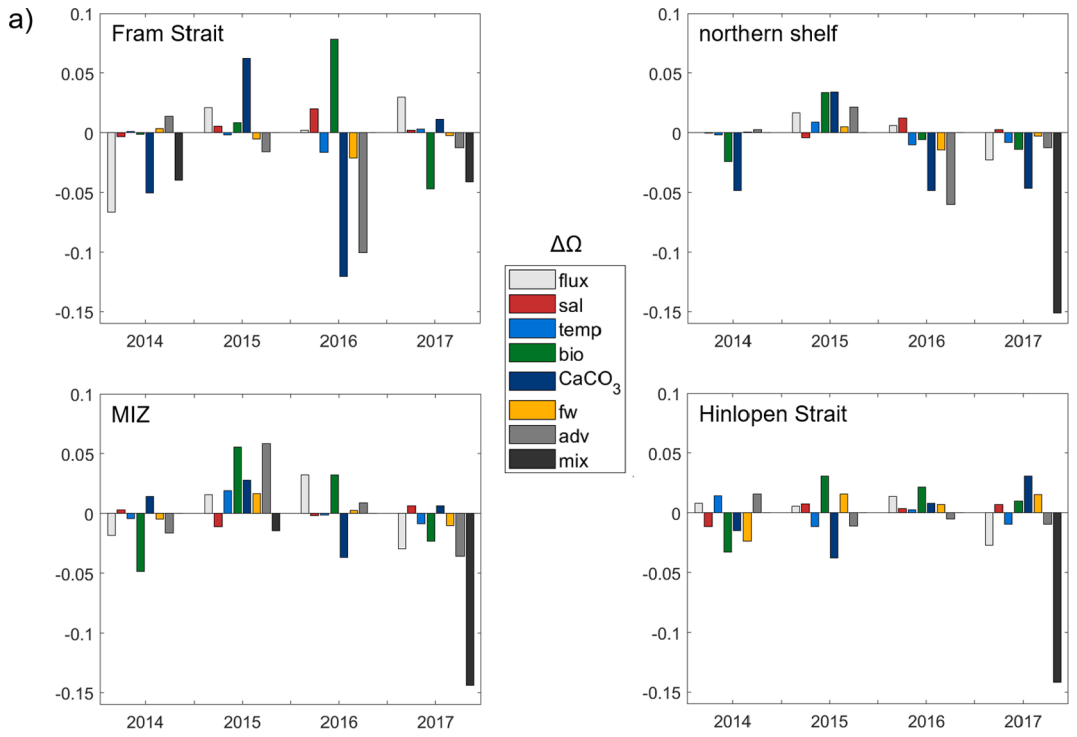

Fig. 11. Anomalies in Ω ($\Delta\Omega = \Omega_{obs} - \Omega_{ave}$) in late summer from mean values in the mixed layer (upper 20 m) in each observation year (Ω_{obs}) relative to the 4-year average (Ω_{ave}) in (a) and relative contribution ($\Delta\Omega$ %) in (b) due to changes in air-sea CO_2 flux ($\Delta\Omega_{flux}$; light grey), salinity ($\Delta\Omega_{sal}$; red), temperature ($\Delta\Omega_{temp}$; light blue), photosynthesis/respiration ($\Delta\Omega_{bio}$; green), $CaCO_3$ mineral formation/dissolution ($\Delta\Omega_{CaCO3}$; dark blue), mineral content of freshwater ($\Delta\Omega_{FW}$; yellow), advection ($\Delta\Omega_{adv}$; grey) and mixing ($\Delta\Omega_{mix}$; black) and for each sub-region: eastern Fram Strait, northern shelf, Hinlopen Strait and the Marginal Ice Zone (MIZ). (For interpretation of the references to color in this figure legend, the reader is referred to the web version of this article.)

µatm and −93 µatm) in all years, notably stronger CO_2 fluxes of −13.3 ± 5.7 mmol m^{-2} day^{-1} in 2014 resulted from higher wind speeds (7.4 ± 4.4 m s^{-1}, with gusts up to 19.7 m s^{-1}) relative to the other years. The strongest oceanic sink of atmospheric CO_2 of 20.5 mmol m^{-2} day^{-1} during the 2014–2017 study period was found in eastern Fram Strait in 2014. This intense CO_2 drawdown resulted from localised processes that created higher A_T, from Atlantic Water intrusions, coupled with reduced C_T, from phytoplankton uptake, in cooler and fresher surface waters. Thereby, an anomalously high influx of CO_2 into the mixed layer induced decreases in Ω ($\Delta\Omega_{flux}$ of −0.07) to represent a key driver of inter-annual variability in Ω in eastern Fram Strait.

Arctic conditions of cold, fresh PSW and summer sea ice cover characterised the MIZ each year, which was a biogeochemically distinct sub-region with the least inter-annual variability in ΔΩ anomalies. With the icescape shifting from consolidated pack, rapid ice retreat and sea-ice melt, the MIZ exhibited the greatest range in freshwater fractions up to ~15 % out of all the regions. Combined with the naturally low [CO_3^{2-}] ~ 120–150 µmol kg^{-1} of Arctic waters, additions of sea-ice and snow melt ($\delta^{18}O$ of −0.09‰) created lower Ω values ~1.9–2.3 across the MIZ. This was especially evident in 2016, where the degree of aragonite saturation was lowered to the 4-year minimum of 1.87 as forced by low [CO_3^{2-}] of 123 µmol kg^{-1} in cold (θ of −1.23 °C) and relatively fresh (S ~ 31.3) PSW. The fresh meltwater with a lower A_T (~205 µmol kg^{-1}) signature compared with surface seawater A_T (~2100 µmol kg^{-1}) exerted a physical (low salinity) and geochemical (low [CO_3^{2-}]) decrease on Ω, which can result in meltwater-induced acidification (Chierici and Fransson, 2009; Fransson et al., 2013, 2015).

The variations in $\delta^{18}O$ in the surface layer revealed spatio-temporal dynamics in freshwater inputs from earlier sea ice melt and Atlantic Water influence (in 2015) to recent sea ice melt and enhanced meteoric influences (in 2016 and 2017). The spatial variability in the freshwater $\delta^{18}O$ signature results from the greater influences of glacial meltwater and river runoff in the coastal areas of Hinlopen Strait (average $\delta^{18}O_{S=0}$ of −5.59‰) and along the northern shelf (average $\delta^{18}O_{S=0}$ of −3.30‰). The freshwater signal in the MIZ reflected less meteoric influence (average $\delta^{18}O_{S=0}$ of −0.88‰) and results from greater inputs from melting sea ice where fractionation in $\delta^{18}O$ occurs during sea ice formation relative to the source seawater. Further fractionation during evaporation and precipitation leads to snow and rain becoming increasingly depleted in $\delta^{18}O$ relative to seawater. Compared with $\delta^{18}O$ values ranging from −16 to −9.8‰ in glacial ice, −17.5 to −5.5‰ in snow and −8.04 to 2.69‰ in sea ice near Tempelfjorden, west Spitsbergen (Fransson et al., 2015, 2020), the $\delta^{18}O$ signature of freshwater (average $\delta^{18}O_{S=0}$ of −2.00‰) of the northern Svalbard shelf and Atlantic Arctic region is largely sea ice melt, with localised influences of glacial meltwater and snow melt, superimposed onto the background oceanic $\delta^{18}O$ signal. The estimated freshwater fraction of A_T indicated that there was a small and spatially-varying A_T source. Freshwater A_T of ~186–192 µmol kg^{-1} in eastern Fram Strait and the northern shelf likely result from advected $CaCO_3$ shells and subsequent incorporation into locally-forming sea ice along the Atlantic Water inflow (Chierici et al., 2019). The higher freshwater A_T component of ~360 µmol kg^{-1} in the MIZ is likely to be a composite signal of dissolution of advected biotic $CaCO_3$ and greater influence of abiotic $CaCO_3$ from sea ice (Fransson et al., 2015). Much higher A_T of ~1000 µmol kg^{-1} in freshwater end-members derived from runoff from Siberian rivers (Fransson et al., 2001; Cooper et al., 2008) could become incorporated into sea ice forming over the Siberian shelf that is subsequently imported and melted in the MIZ north of Svalbard. The regionally-averaged freshwater A_T of ~205 µmol kg^{-1} determined for the Atlantic-Arctic region in 2014–2017 may reflect the large variability of A_T in sea ice and integrate signals of dissolution of northward advected $CaCO_3$ shells (Chierici et al., 2019) and terrestrial dissolved minerals in glacial meltwater, i.e., more relevant for Hinlopen Strait and the northern shelf waters (Fransson et al.,

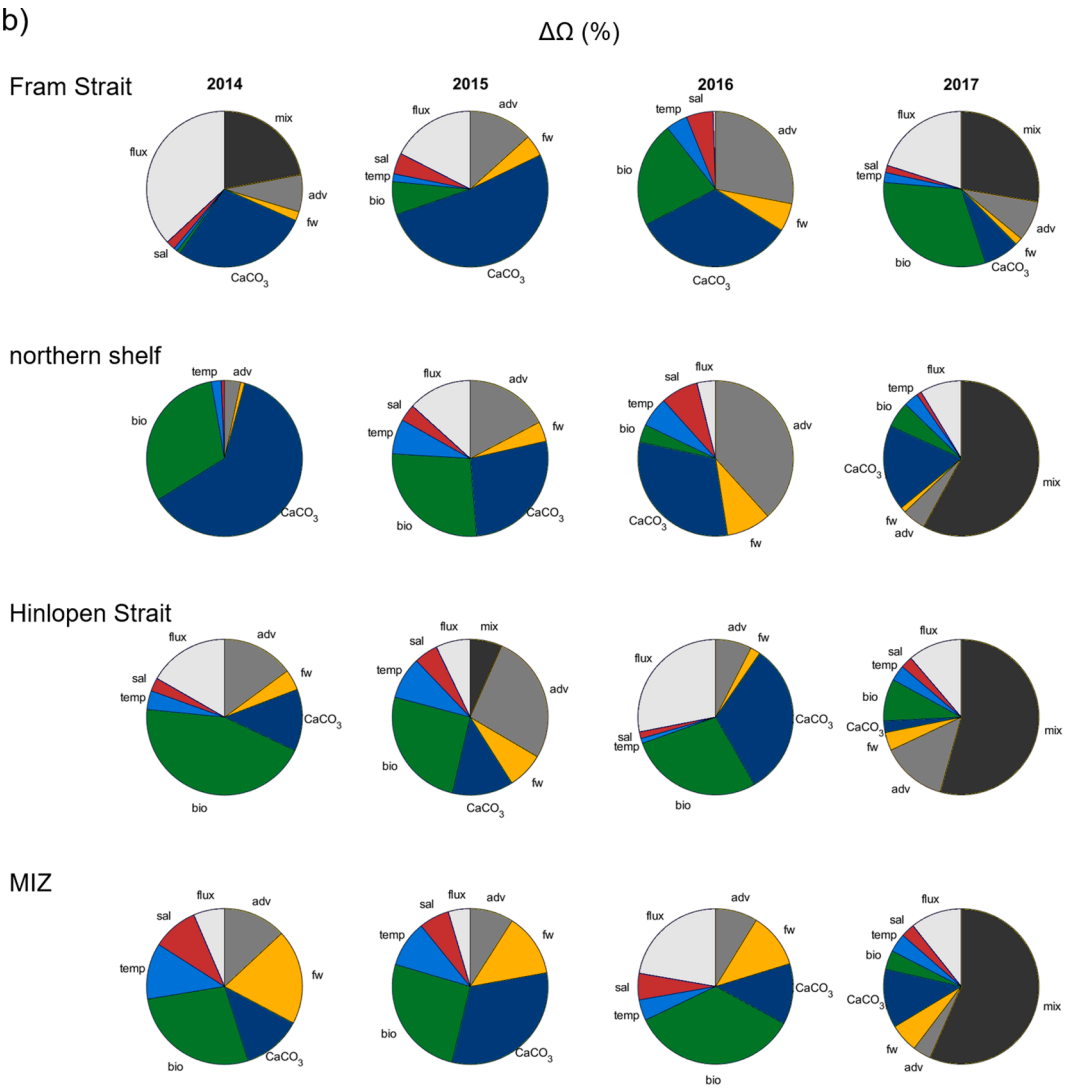

Fig. 11. (*continued*).

2015, 2020; Ericson et al., 2018, 2019a). The freshwater endmember is similar in magnitude to 315 μmol kg^{-1} as estimated for sea-ice melt by Chierici et al. (2019) and would constitute a minor buffer against dilution effects in surrounding surface seawater across the region.

In the years of earlier (2015) and rapid (2016, 2017) sea ice retreat in the MIZ, dilution effects reduced C_T and A_T with net increases in Ω from positive $\Delta\Omega_{sal}$ anomalies of ~0.01. These salinity effects were accompanied by positive $\Delta\Omega_{FW}$ anomalies of ~0.02 that accounted for about 13% of the total ΔΩ in the MIZ and suggest that ice-derived carbonate ions from ikaite dissolution played a minor but consistent role in supplying A_T to surface waters. As sea-ice meltwater was the dominant freshwater source to the region, A_T of 205 μmol kg^{-1} included contributions from $CaCO_3$ within the ice, i.e. ikaite. It is expected that any ikaite in the ice would dissolve during melting and analysis (Fransson et al., 2020 and references therein) and, therefore, that the majority of the A_T sourced from ikaite is transferred from the ice to surface waters, enhancing surface water Ω and buffering against meltwater-induced acidification. In comparison, the negative $\Delta\Omega_{FW}$ anomaly (−0.02) representing 20% of the total ΔΩ in the MIZ in 2014 signals the opposing effect of less sea ice melt and thus less ice-derived carbonates in late summer surface waters of the MIZ. Furthermore, decreases in A_T due to dilution effects were slightly counteracted by increases in A_T as a result of photosynthetic CO_2 uptake (positive $\Delta\Omega_{bio}$) and $CaCO_3$ dissolution (positive $\Delta\Omega_{CaCO3}$).

Significant relationships between freshwater fractions and Ω in surface waters (Table 5) showed that for a 10% increase in freshwater, surface waters with Arctic-like conditions (2014) experienced a reduction in Ω of 0.28 compared with Atlantic-like (2015) conditions where surface water Ω was reduced by 0.16 (Fig. 12). For the years 2016 and 2017, the transition from ice covered to ice free waters revealed that reductions in surface water Ω were slightly lower than those in 2014 with rates of 0.025/FW% and 0.026/FW%, respectively (Table 5). These values fall within the ranges of reductions in summer surface water Ω reported for fjords of west Svalbard: Isfjorden (0.009/FW%; Ericson et al., 2019b) and Kongsfjorden (0.7/FW%; Fransson et al., 2016). The warmer, more Atlantic-like conditions in 2015 showed that freshwater exerted the smallest control on late summer surface water Ω, whereby a freshwater contribution of ~88% would lead to lowering of Ω to acidification levels. Contrastingly, the colder, fresher surface waters in 2016 were more vulnerable to lower Ω as freshwater contributions of ~48% could drive acidification of surface waters.

The signature of low Ω, from the naturally low [CO_3^{2-}], is typical of Arctic waters influenced by melting sea ice and meteoric waters where surface water acidification has already been documented across the Arctic (e.g., Chierici and Fransson, 2009; Yamamoto-Kawai et al., 2009). Future warming is suggested to have significant impacts on freshwater fluxes in the Arctic region through increased sea-ice melt and glacial meltwater release (Fransson et al., 2016; Hopwood et al., 2020). Greater

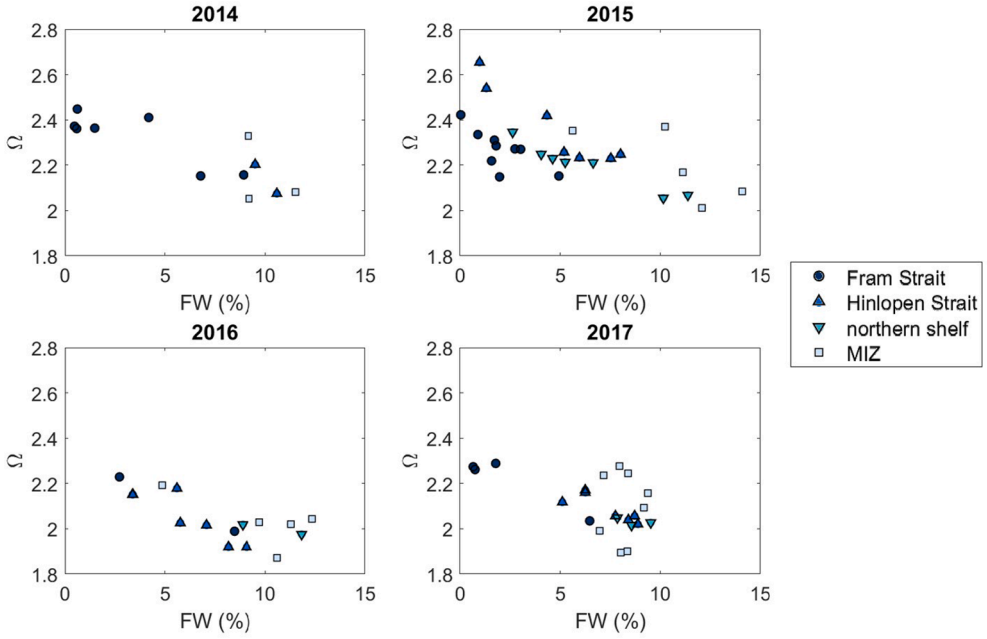

Fig. 12. Relationships between freshwater fraction (FW) and Ω in surface waters (upper 10 m) of eastern Fram Strait (open circles), Hinlopen Strait (triangles), northern shelf (downward triangles) and the MIZ (open squares) per year (2014, 2015, 2016, 2017).

runoff is likely to contribute dissolved minerals of terrestrial origin and sediments, which will reduce light availability and limit primary production in the surrounding coastal waters. In addition, more organic matter is likely to be transport and released, which will elevate CO_2 in the water column upon remineralisation. Future changes with more freshwater and oceanic uptake of atmospheric CO_2 result in lowering of Ω that enhances the vulnerability of organisms such as the pteropod *L. helicina* in the Svalbard and Arctic Ocean region.

4.2. Atlantic-like regime and biologically-driven effects on acidification states

Highest surface layer Ω (2.26 ± 0.14), with maximum values of 2.65 along the northern shelf, occurred in the relatively warm and low-ice summer of 2015. The elevated degree of aragonite saturation across all regions constituted physical, biological and biogeochemical buffers against ocean acidification. The ice edge at ~82°N was approximately 110 km farther north than in 2014 and thus exposed surface waters to solar heating and favourable light levels for a longer duration by late summer. Compared with the other years, the water column in 2015 was less stratified with reduced meltwater influence and increased wind-driven mixing in the larger expanse of open water. A more saline surface layer with salinity of ~32.98 and elevated $\delta^{18}O$ of ~0.45‰ in 2015, compared to 2016 (S of ~32.37 and $\delta^{18}O$ of ~0.11) and 2017 (S of ~32.64 and $\delta^{18}O$ of ~−0.02), traced the greater influence of Atlantic Water on the surface layer. The PSWw was more widespread with generally higher temperatures in the upper water column. The Arctic-like PSW was localised to the upper 100 m only in the northern ice-covered MIZ. The inter-annual Ω variability in the mixed layer in 2015 was strongly driven by phytoplankton production and biological fixation of C_T into organic matter, with $\Delta\Omega_{bio}$ ranging from 0.01 to 0.06 and accounting for ~25% of the total ΔΩ in the sub-regions except Fram Strait. Chlorophyll concentrations up to 4.03 mg m^{-3} indicated ongoing late-summer phytoplankton production with associated increases in $[CO_3^{2-}]$ and in Ω.

The uptake and cycling of C_T, NO_3 and PO_4 were generally closely coupled, with deviations at lower respective concentrations due to the overconsumption of carbon, and PO_4, at near-depleted NO_3. This was reflected in the annually high C:N uptake ratios (>20) in the mixed layer that result from ongoing C_T drawdown under low NO_3 or NO_3 limiting conditions, as reported during seasonally-resolved studies in a west Svalbard fjord (Ericson et al., 2019b). Comparatively lower C:N and higher N:P uptake ratios in 2015 are indicative of later stage bloom conditions where NO_3 re-supply and recycling through organic matter remineralisation alleviates transient limitation to sustain C_T drawdown. The variation of inorganic carbon and nutrient cycling from different water mass contributions has previously been reported by Frigstad et al. (2014) who found lower C:N uptake ratios of 6.7 in Atlantic Water regimes compared to 7.9 for Arctic waters in the Barents Sea. Similarly, Ericson et al. (2019b) found lower C:N of 6.6 ± 0.5 with greater proportions of Atlantic Water compared with C:N ratios of 8.7 ± 0.6 with more Arctic water in a west Svalbard fjord. The C:N uptake ratios in Atlantic Water influenced regions exceed the classical Redfield stoichiometry (Redfield et al. 1963), with respect to carbon, also reflect air-sea CO_2 uptake and the influx of C_T into surface waters during drawdown of atmospheric CO_2.

Concentrations of $Si(OH)_4$ were usually above 0 μmol kg^{-1} in contrast to depleted NO_3, yielding Si:N uptake ratios of 0.33 in the mixed layer. This is indicative of the drawdown of macronutrients from non-siliceous phytoplankton species, such as the haptophyte *Phaeocystis pouchetii*, followed by changes in community composition and $Si(OH)_4$ uptake in diatom blooms (Assmy et al., 2017). The phytoplankton communities during late summer were likely diatom-dominated and acclimatised to warm, thermally-stratified and low-nutrient conditions (Le Fouest et al., 2011; Rainville et al., 2011; Oziel et al., 2017; Henley et al., 2020). The Atlantic Water inflow region can become nitrate limited during the growing season (Kattner and Becker, 1991; Randelhoff et al., 2018) whereby over-consumption of C_T relative to nitrate commonly occurs (Chierici et al., 2011; Ericson et al., 2019b). The late-summer ecosystem could evolve into a nutrient-recycling state, whereby remineralisation takes place in the upper water column (Randelhoff et al., 2018) and rates of net community production decrease (Chierici et al., 2019). Mixing into subsurface Atlantic Water likely re-supplied the euphotic zone to alleviate any NO_3 limitation (Randelhoff et al., 2015; Slagstad et al., 2015; Tremblay et al., 2015), thus extending the growing season in 2015. This is opposite to findings of increased Atlantic Water, or modified Atlantic Water, resulting in reduced biological CO_2 uptake compared with earlier onset of the bloom and greater seasonal

drawdown in the presence of more Arctic water in Adventfjorden, west Svalbard (Ericson et al., 2019b). This likely results from a balance of the respective contributions of the low-C_T (productive) and low-A_T (fresher) Arctic waters versus the high-C_T (anthropogenic CO_2) and high-A_T (saline) Atlantic Water.

Positive $\Delta\Omega_{flux}$ of 0.01–0.02 in all regions in 2015 reflects increased mixed layer Ω due to anomalously low atmospheric CO_2 uptake. Incoming radiation and influence of warm Atlantic Water results in a thermodynamic increases in pCO_2 and decreases in pH_T in the surface layer (Millero, 2007; Takahashi et al. 1993). For a + 1 °C change in seawater temperature, pCO_2 is raised by approximately 10 μatm (Takahashi et al. 1993). Thus, an increase of 0.5–2.5 °C in regionally-averaged surface water temperatures in 2015, relative to the other years, would be expected to raise pCO_2 by ~5–25 μatm. Regionally-averaged surface water pCO_2 had little variation in 2014, 2016 and 2017 of 209–212 μatm in contrast to the highest regionally-averaged pCO_2 of 227 μatm in 2015. Therefore, warmer Atlantic-like conditions exerted a small thermodynamic control on surface water pCO_2 and a reduction in the air-sea CO_2 gradient. Coupled to lower wind speeds, these effects weakened the amount of atmospheric CO_2 uptake and resulted in less CO_2 flux-driven increases in mixed layer C_T. The extent of biological carbon drawdown in the advanced phase bloom conditions of 2015 was also reflected by elevated pH_T of 8.25 over the northern shelf. The biologically-driven CO_2 undersaturation was slightly eroded in the warmer PSWw and Atlantic Water-influenced mixed layer relative to the stronger undersaturation (142 μatm) and higher pH_T (8.40) that occurred in the coldest and freshest ice-influenced waters in the MIZ in 2015. This natural spatial variability in 2015 was also reflective of the temporal variability in comparison to the generally colder, ice-influenced conditions of 2014, 2016 and 2017.

Photosynthetic uptake of CO_2 is a dominant control for biogeochemical cycling on a wider regional scale from the glacial meltwater-influenced fjords in west Spitsbergen (Fransson et al., 2016; Ericson et al., 2019a) and the Fram Strait region of the Atlantic Water inflow (Chierici et al., 2019) to the sea ice influenced Amundsen Gulf, Beaufort Sea (Chierici et al. 2011). Increases in primary production over recent decades have been attributed to reductions in the areal extent of sea ice that increase the phytoplankton productive season in the Atlantic Water inflow region and wider Arctic Ocean (Carmack et al., 2006; Wassmann et al., 2006; Arrigo and van Dijken, 2015). Warming, sea ice loss and increased advection of Atlantic Water, or "Atlantification", has significantly altered the sea scape (Onarheim et al., 2014; Carmack et al., 2015; Polyakov et al., 2017) where increased primary production (Reigstad et al., 2002; Slagstad et al., 2015) affects nutrient cycling (Henley et al., 2020), net community production and atmospheric CO_2 uptake (Chierici et al., 2019). A shift to an Atlantic-like regime as indicated by observations in 2015 is fundamental in creating more ice-free conditions that impacts the biological forcing (biological-physical "Atlantification") on ocean acidification states in the Atlantic-Arctic Ocean.

4.3. Atlantic-like regime and geochemical buffering against acidification

The more Atlantic-like environment in 2015 shaped the biogeochemical characteristics of the surface layer as subsurface water increased A_T by ~15–50 μmol kg^{-1} to generate the highest regionally averaged values of 2215 ± 90 μmol kg^{-1} during 2014–2017. The balance of competing processes that influenced C_T and A_T supplied from incursions of Atlantic Water led to large spatio-temporal heterogeneity in Ω in the upper water column. Surface water Ω in 2015 exhibited the greatest range from 2.01 to 2.65 across the whole region compared with the other years. Enhanced A_T from $CaCO_3$ processes ($\Delta\Omega_{CaCO3}$; between −0.04 and 0.06) and advection ($\Delta\Omega_{adv}$; between −0.02 and 0.06) were key drivers and accounted for ~52% and ~27%, respectively, of Ω variability in 2015. Alongside biological production, these processes further contributed to increased Ω as buffers against acidification, i.e., geochemical "Atlantification".

Increases in mixed layer Ω from $CaCO_3$ dissolution can occur from advection and mixing with different water masses where dissolution of biotic $CaCO_3$, with contributions from abiotic $CaCO_3$ (ikaite) from melting sea ice, has taken place (Rysgaard et al., 2012; Fransson et al., 2013; Oziel et al., 2020). However, as sea ice had departed earlier in 2015 (with the exception of the MIZ), contributions from ice-derived $CaCO_3$ are envisaged to be to minor. The role of ikaite in the inter-annual variability in $\Delta\Omega_{CaCO3}$, particularly in the MIZ, is discussed in section 4.4. Calcifying phytoplankton, e.g., coccolithophores (calcitic tests), and zooplankton, e.g., pteropods (aragonitic shells), are ubiquitous in pelagic ecosystems (e.g., Bednaršek et al., 2019). The range of the coccolithophore Emiliania huxleyi has expanded northwards and these phytoplankton can maintain growth under low nutrient conditions (Hegseth and Sundfjord, 2008; Oziel et al., 2020). Calcifying zooplankton represent a large fraction of total zooplankton biomass and are major producers of $CaCO_3$ and, together with coccolithophores, are important regulators of pelagic inorganic carbon fluxes (e.g., Berner and Honjo, 1981; Bednaršek et al., 2012). The chemical imprint of $CaCO_3$ dissolution results from local formation/dissolution or from the advection of $CaCO_3$ shells from upstream in the Atlantic Water inflow (Chierici et al., 2019; Oziel et al., 2020). The transport of pelagic organisms in the WSC and boundary current along the shelf to the west and north of Svalbard, which following dissolution, likely contributed to increased water column [CO_3^{2-}] up to 176 μmol kg^{-1}. These processes led to positive $\Delta\Omega_{adv}$ anomalies. The dominance of PSWw (4-year average Ω of 2.08 ± 0.28) over PSW (4-year average Ω of 1.92 ± 0.34) in 2015 was key in driving higher Ω of 2.28 ± 0.14 in the warmer surface layer. Concomitant increased C_T (4-year average 2158 ± 19 μmol kg^{-1}) and the impact of the low-Ω (4-year average 1.68 ± 0.22) signature of Atlantic Water likely resulted in an ephemeral offset to the biologically-driven increases in Ω. However, in the presence of NO_3 supply and active late summer phytoplankton communities, ongoing C_T uptake retained higher Ω. Contributing A_T to productive waters enhances the buffering capacity (increased A_T and decreased C_T) and upholds elevated Ω. These processes of geochemical-physical "Atlantification" provide mechanisms to strengthen the buffer against acidification in Atlantic-like regimes.

4.4. Acidification states in the transition from ice-covered to meltwater-influenced surface waters

Relative to all 4 years, lowest surface water Ω of 2.05 ± 0.10 and 2.11 ± 0.12 occurred in the colder and ice-influenced waters in 2016 and 2017, respectively. The lower Ω was the result of numerous negative ΔΩ anomalies (except in the MIZ) that enhanced the vulnerability of the surface layer to acidification. The largest differences between positive and negative anomalies, i.e. ΔΩ amplitudes, were 0.20 in 2016 and 0.18 in 2017, which resulted from competing processes driving both large increases and decreases in Ω. The corresponding ΔΩ amplitude in 2014 was 0.09 and in 2015 was 0.10, reflecting the predominantly negative and positive anomalies in the respective years. Reductions in mixed layer Ω in 2016 and 2017 were driven by the dominance of negative $\Delta\Omega_{adv}$ anomalies between −0.10 and 0.01; up to ~38% of total ΔΩ. Sea ice covered most of the region in August 2016 and 2017, which resulted in a relatively delayed and rapid retreat of the ice pack by September and created a transitional Arctic-Atlantic domain. The lower average $\delta^{18}O$ values, i.e, −0.02 ± 0.30‰ in 2017, were indicative of snow melt (accumulated on sea ice) and glacial meltwater mixed into the larger background signal of sea-ice melt and seawater. The patterns in shifting ice cover and greater meltwater influence along the Atlantic Water inflow are reflected in the variability of A_T and C_T. Freshwater contributions were greatest in 2016 and 2017, which were accompanied by lowest surface water C_T and A_T (4-year minima found in 2016) of 1863 μmol kg^{-1} and 2061 μmol kg^{-1}, respectively. The greater control of salinity changes on A_T, relative to C_T, was reflected in [CO_3^{2-}] as surface

water concentrations were lowest at 135 ± 7 μmol kg^{-1} in 2016 compared with highest [CO_3^{2-}] of 149 ± 9 μmol kg^{-1} in 2015. This resulted in anomalously low [CO_3^{2-}] to drive suppression of Ω in the sea-ice and meltwater-influenced conditions.

In most regions in 2016 and 2017, the negative $\Delta\Omega_{adv}$ anomalies were accompanied by small and negative $\Delta\Omega_{temp}$ anomalies (lowest of −0.02). These temperature effects result from the imprint of recently ice-covered and meltwater affected surface waters. A decrease of ~0.5 °C increases C_T by ~3 μmol kg^{-1} and thermodynamic reductions in Ω result as the solubility of aragonite increases in cooled seawater (Mucci, 1983). Counteracting the effects of temperature, small and positive $\Delta\Omega_{sal}$ anomalies (up to 0.02) resulted from dilution of both C_T and A_T from the meltwater inputs. Reduced C_T had the greater influence on the Ω resulting in net increased Ω. In 2016, anomalously low A_T inputs from $CaCO_3$ processes (except in the MIZ) created $\Delta\Omega_{CaCO3}$ between −0.12 and −0.04. Conversely in 2017, elevated A_T generated positive $\Delta\Omega_{CaCO3}$ anomalies (except over the northern shelf) ranging from 0.01 to 0.03. The largest negative $\Delta\Omega_{CaCO3}$ anomalies in 2016 were found in the stratified waters recently influenced by sea ice melt and in eastern Fram Strait that show lower Ω from reduced $CaCO_3$ dissolution relative to the 4-year average. This is likely to result from less Atlantic Water influence, as such the higher [CO_3^{2-}] from the breakdown of exported $CaCO_3$ shells in subsurface waters was not integrated into the surface layer.

The Arctic-like conditions in 2016 had greater stratification from recent meltwater inputs. PSW was confined to a shallow meltwater lens up to about 10 m deep and Atlantic Water was retained below ~50 m depth. Surface water CO_2 was most undersaturated, with a regionally-averaged value of 209 ± 35 μatm in the colder surface waters. However, lowest wind speeds (5.3 ± 3.6 m s^{-1}) relative to the 4-year average weakened the oceanic sink for atmospheric CO_2 to 11.1 ± 35 mmol m^{-2} day^{-1}, which indicated that some waters were a CO_2 source in this region, resulting in positive $\Delta\Omega_{flux}$ anomalies (0.01–0.03), i.e. anomalously low C_T inputs from the atmosphere. Advanced sea ice retreat and earlier onset of Atlantic-like conditions in 2016, relative to 2017, created a pulse of late summer phytoplankton production. Meltwater-induced stratification promoted phytoplankton production in favourable light conditions to drive anomalously high biological carbon uptake (except over the northern shelf) with $\Delta\Omega_{bio}$ of 0.02–0.08. The biological C_T drawdown was a key control in decoupling the ocean acidification variables as, in contrast to [CO_3^{2-}] and Ω, the fresher surface waters were accompanied by higher pH_T in 2016. The following year reflected a comparatively delayed phase, where the later retreat of the summer sea ice in 2017 had yet to lead to widespread freshening, therefore salinity-driven variations in [CO_3^{2-}], Ω and pH_T were similar to those of ice-associated (more Arctic-like) waters in 2014. Conversely, anomalously low biological production (except in the MIZ) yielded $\Delta\Omega_{bio}$ between −0.05 and −0.01. This biological effect reflects more Arctic-conditions, where a reduced light- and lower meltwater-driven biological response resulted in anomalously low Ω.

Vertical mixing dominated the variability in mixed layer Ω in 2017 (27–58% of total ΔΩ for all sub-regions) as intrusions of low-Ω Atlantic Water resulted in $\Delta\Omega_{mix}$ between −0.15 and −0.04. Atmospheric forcing from warmer air temperatures and high wind speeds likely contributed to rapid degradation of the sea ice and resultant deeper mixed layers across the region. Recently open surface waters and wind-driven mixing allowed C_T, A_T and nutrients to infuse the upper water column. Intrusions of Atlantic Water (negating effects of increased A_T supply) created strong, negative $\Delta\Omega_{mix}$ anomalies across the whole region. The $\Delta\Omega_{mix}$ anomalies likely represented a transitory scenario based on instantaneous depths of the active mixing layer at the time of sampling and the transfer of low-Ω Atlantic Water into the higher-Ω PSW/PSWw layers. The immediate effect is a ephemeral reduction in surface layer Ω. However, the supply of A_T from the Atlantic Water (4-year average 2317 ± 9 μmol kg^{-1}) acts as a geochemical buffer to offset this effect, which is accounted for in the advection estimates. As such, the small negative $\Delta\Omega_{adv}$ anomalies in 2017 reflect the net effect of the horizontal input of higher C_T and lower A_T waters of Arctic origin, that also reduced Ω. Accompanied by negative $\Delta\Omega_{bio}$ from a reduced photosynthetic uptake signal, these processes become superimposed to further lower the mixed layer Ω in 2017.

The effects of recent and rapid ice retreat and deep mixed layers in 2017, resulted in colder, fresher PSW layer that extended from the surface to the sea floor (250–450 m deep) over the shallow shelf around Nordaustlandet. The Atlantic-derived component of the water masses observed around Nordaustlandet may also have been advected into the area from the south in the Barents Sea, as opposed to advection through the boundary current and the northern Atlantic Water branch. The biogeochemical signatures of the bottom waters were at the upper bounds of a saline (~34.5) PSW with $\delta^{18}O$ of 0.37–0.48, C_T ~ 2165 μmol kg^{-1}, A_T ~ 2290 μmol kg^{-1}, and Ω of 1.29–1.38. The more acidified PSW could result from local sea-ice processes where rejected CO_2-rich brines enrich subsurface waters with C_T (Fransson et al., 2013; Ericson et al., 2019b) and/or mixing with the Coastal Current, that has been observed to have elevated C_T content from sea-ice brines (Fransson et al., 2016).

4.5. Acidification signals in Atlantic Water and Arctic Intermediate Water

To investigate processes that influenced the Ω in the Atlantic Water across the Atlantic-Arctic region in 2014–2017, repeat stations in eastern Fram Strait at 78.0 °N 9.5 °E (Fig. 1b) that represent the inflowing Atlantic Water core (50–500 m) were evaluated. Inter-annual variability in water masse structure likely played a role given that salinities in the Atlantic Water core ranged from 35.13 (less sea-ice melt influence) in 2014 to 35.00 (more sea-ice melt freshening) in 2017. Values of A_T were2316-2320 μmol $kg^{-1}$and likely resulted from salinity variations and/or inorganic $CaCO_3$ dissolution, with higher A_T and Ω in 2015. Phytoplankton production reduced C_T and increased Ω; lowest C/N of 4.1 in 2015 was indicative of more advanced-stage blooms, with drawdown of C_T and NO_3 versus mixing and resupply processes. Higher C_T and lower NO_3 (higher C/N of 6.6) is indicative of early-stage bloom conditions in 2017. Enhanced organic matter remineralisation would elevate C_T and suppress Ω in the Atlantic Water upon passage north-west during/following the growing season. Likely temporal variability in the inflowing Atlantic Water and the greater influence of Atlantic Water in the water column along the inflow shelves, as determined from thicker Atlantic Water layers (defined by potential temperature - salinity characteristics) and shoaling intrusions, were key mechanisms in creating a higher buffering capacity and elevated Ω in the Atlantic-Arctic region in 2015.

A similar pattern in the AIW revealed year-to-year deviations when compared with the Ω 4-year average of 1.20 ± 0.10. In eastern Fram Strait and at the shelf break at Hinlopen Strait, Ω of ~1.20 was found at 800–1200 m. Over the northern shelf, the AIW layer had deepened to 1000–2100 m with accompanying Ω of ~1.12. The AIW in the MIZ was found over a greater depth range of 700 m to 2630 m with the aragonite saturation horizon at 1800–2230 m depth in the Nansen Basin. For the Atlantic and intermediate layers (~100–1500 m) in the Nansen Basin, Ericson et al. (2014) reported decreases in Ω by 0.05–0.14 (Ω starting at ~1.2–1.4) during 1994–2011 and Ulfsbo et al. (2018) determined similar reductions of 0.04–0.06 in Ω during 1996–2015. In the MIZ, the northern limit at ~82 °N, AIW at 1500 m depth had Ω of 1.13 ± 0.02 in 2015. From simplistic calculations, an estimated decrease in Ω in the AIW in the Nansen Basin was ~0.07 in two decades, following Ericson et al. (2014). This rate of decrease in Ω at the deeper limit of intermediate waters supports those proposed previously. Inflowing Atlantic Water into intermediate levels of the Nansen Basin entrains remineralisation signals and sequesters anthropogenic CO_2 from atmospheric uptake in the Atlantic Ocean. The decline in Ω has been attributed to accumulation of C_T from increasing anthropogenic carbon in the Atlantic Water inflow into the Arctic Ocean (Ericson et al., 2014; Ulfsbo

et al., 2018). Therefore, intermediate layers of the Atlantic Arctic Ocean in the Nansen Basin could experience aragonite undersaturation in the next 50–100 years.

5. Concluding remarks and future outlook

The inflow of Atlantic Water through eastern Fram Strait and along the northern Svalbard shelf encounters the seasonally-ice covered Arctic waters that create a dynamic region of intricately linked processes that influence the state of ocean acidification in the region. Inter-annual variability in late summer Ω in the surface layer was driven by variations in sea ice cover and meltwater inputs, phytoplankton production, $CaCO_3$ processes and advection/mixing of different water masses. Reduced extent of summer sea ice cover was linked to greater Atlantic Water influence, whereby an extended duration of phytoplankton production and biologically-induced increases in Ω dominated the inter-annual variability in acidification states. Highest Ω was prevalent in the surface layer in Atlantic-like conditions, where Atlantic Water increased [CO_3^{2-}] to enhance the buffer capacity in the presence of primary production to compensate the C_T enrichment. Pelagic calcifying plankton (aragonite, calcite) and sea-ice derived $CaCO_3$ (ikaite) were sources of [CO_3^{2-}] upon dissolution, which increased Ω in the Atlantic Water- and meltwater-influenced surface waters, respectively. Rapid retreat of the ice pack created Arctic-like conditions through meltwater-driven stratification and dilution of [CO_3^{2-}] that limited advection of Atlantic Water and reduced biological C_T drawdown, which lowered Ω. Dissolution of ikaite in sea ice acted as a small geochemical buffer in meltwater-influenced surface waters. Wind-driven mixing and incursions of low-Ω Atlantic Water into the upper water column led to transient acidification signals in the surface layer. Surface waters across the region were strongly undersaturated with respect to atmospheric CO_2, creating substantial oceanic CO_2 sinks that lowered Ω in ice-free waters.

There is a balance of competing effects on Ω in the Atlantic-Arctic region, whereby increased Atlantic Water influence drives (i) ice-free waters and reduced dilution (physical increases in Ω), less sea-ice derived $CaCO_3$ (geochemical decreases in Ω), nitrate re-supply to sustain primary production (biological increases in Ω) and enhanced A_T (geochemical increases in Ω) versus (ii) increased C_T from higher anthropogenic CO_2 content (chemical decreases in Ω), wind-driven mixing (physical decreases in Ω) and remineralisation of organic matter (biological decreases in Ω). Understanding the consequences of "Atlantification" and changing meltwater fluxes on the marine carbonate system is critical to better predict the impacts on biogeochemical cycling and functioning of the ecosystem in a changing Arctic Ocean.

Declaration of Competing Interest

The authors declare that they have no known competing financial interests or personal relationships that could have appeared to influence the work reported in this paper.

Acknowledgments

We gratefully acknowledge the assistance provided by the Captain and Crew of the R/V *Helmer Hanssen* and assistance from numerous scientists aboard for their help during the field campaigns. The CarbonBridge project was funded by the Research Council of Norway (RCN 226415). SI-ARCTIC (Strategic Initiative – The Arctic Ocean Ecosystem) is a 5-year (2014–2018) strategic initiative at the Institute of Marine Research funded by the Ministry of Trade, Industry and Fisheries through the Research Council of Norway (RCN 228896). We are also grateful for the support from the Flagship program "Ocean Acidification and effects in northern waters" within the FRAM-High North Research Centre for Climate and the Environment. Data for this paper will be available from the Norwegian Marine Data Centre (NMDC). Thanks to the Norwegian Meteorological Institute for the data from Svalbard Airport and to NILU for the atmospheric CO_2 data that is available from the EBAS data base (http://ebas.nilu.no). The work is a contribution to the Barents Sea Programme at IMR. The authors are very grateful for comments from two anonymous reviewers that have substantially improved the quality of the manuscript.

References

Aagaard, K., Foldvik, A., Hillman, S.R., 1987. The West Spitsbergen Current: Disposition and water mass transformation. J. Geophys. Res. 92C4, 3778–3784.

Ambrose, D., Lawrenson, I.J., 1972. The vapor pressure of water. J. Chem. Thermody. 45, 755–761. https://doi.org/10.1016/0021-96147290049-3.

Anderson, L.G., Macdonald, R.W., 2015. Observing the Arctic Ocean carbon cycle in a changing environment. Polar Res. 341, 26891. https://doi.org/10.3402/polar.v34.26891.

Anderson, L.G., Jutterström, S., Hjalmarsson, S., Wåhlström, I., Semiletov, I.P., 2009. Out-gassing of CO_2 from Siberian Shelf seas by terrestrial organic matter decomposition. Geophys. Res. Lett. 36, L20601. https://doi.org/10.1029/2009GL040046.

Arrigo, K.R., van Dijken, G.L., 2015. Continued increases in Arctic Ocean primary production. Prog. Oceanogr. 136, 60–70. https://doi.org/10.1016/j.pocean.2015.05.002.

Årthun, M., Eldevik, T., Smedsrud, L.H., Skagseth, Ø., Ingvaldsen, R.B., 2012. Quantifying the influence of Atlantic heat on Barents Sea Ice variability and retreat. J. Clim. 25, 4736–4743. https://doi.org/10.1175/JCLI-D-11-00466.1.

Asbjørnsen, H., Årthun, M., Skagseth, Ø., Eldevik, T., 2020. Mechanisms Underlying Recent Arctic Atlantification. Geophys. Res. Lett. 47 https://doi.org/10.1029/2020GL088036.

Assmy, P., Fernández-Méndez, M., Duarte, P., Meyer, A., Randelhoff, A., Mundy, C.J., Olsen, L.M., Kauko, H.M., Bailey, A., Chierici, M., Cohen, L., 2017. Leads in Arctic pack ice enable early phytoplankton blooms below snow-covered sea ice. Sci. Rep. 7, 40850. https://doi.org/10.1038/srep40850.

Bates, N.R., Moran, S.B., Hansell, D.A., Mathis, J.T., 2006. An increasing CO_2 sink in the Arctic Ocean due to sea-ice loss. Geophys. Res. Lett. 33, L23609. https://doi.org/10.1029/2006GL027028.

Bednaršek, N., Mozina, J., Vogt, M., O'Brien, C., Tarling, G.A., 2012. The global distribution of pteropods and their contribution to carbonate and carbon biomass in the modern ocean. Earth System Science Data 41, 167–186. https://doi.org/10.5194/essd-4-167-2012.

Bednaršek, N., Feely, R.A., Howes, E.L., Hunt, B.P., Kessouri, F., León, P., Lischka, S., Maas, A.E., McLaughlin, K., Nezlin, N.P., Sutula, M., 2019. Systematic Review and Meta-Analysis Toward Synthesis of Thresholds of Ocean Acidification Impacts on Calcifying Pteropods and Interactions with Warming. Front. Mar. Sci. 6, 227. https://doi.org/10.3389/fmars.2019.00227.

Berner, R.A., Honjo, S., 1981. Pelagic sedimentation of aragonite: its geochemical significance. Science 211, 940–942.

Beszczynska-Moller, A., Fahrbach, E., Schauer, U., Hansen, E., 2012. Variability in Atlantic water temperature and transport at the entrance to the Arctic Ocean, 1997–2010. ICES J. Mar. Sci. 69, 852–863. https://doi.org/10.1093/icesjms/fss056.

Brewer, P.G., Goldman, J.C., 1976. Alkalinity changes generated by phytoplankton growth. Limnol. Ocean. 21, 108–117. https://doi.org/10.4319/lo.1976.21.1.0108.

Butterworth, B.J., Miller, S.D., 2016. Air-sea exchange of carbon dioxide in the Southern Ocean and Antarctic marginal ice zone. Geophys. Res. Lett. 4313, 7223–7230.

Carmack, E., Barber, D., Christensen, J., Macdonald, R., Rudels, B., Sakshaug, E., 2006. Climate variability and physical forcing of the food webs and the carbon budget on panarctic shelves. Prog. Oceanogr. 71, 145–181. https://doi.org/10.1016/j.pocean.2006.10.005.

Carmack, E., Polyakov, I., Padman, L., Fer, I., Hunke, E., Hutchings, J., Jackson, J., Kelley, D., Kwok, R., Layton, C., Melling, H., 2015. Toward quantifying the increasing role of oceanic heat in sea ice loss in the new Arctic. Bull. Am. Met. Soc. 9612, 2079–2105.

Chen, C.-T.-A., Borges, A.V., 2009. Reconciling opposing views on carbon cycling in the coastal ocean: continental shelves as sinks and near-shore ecosystems as sources of atmospheric CO_2. Deep-Sea Res. II 56, 578–590. https://doi.org/10.1016/j.dsr2.2009.01.001.

Chen, B., Cai, W.-J., Chen, L., 2015. The marine carbonate system of the Arctic Ocean: assessment of internal consistency and sampling considerations, summer 2010. Mar. Chem. 176, 174–188. https://doi.org/10.1016/j.marchem.2015.09.007.

Chierici, M., Fransson, A., 2009. $CaCO_3$ saturation in the surface water of the Arctic Ocean: undersaturation in freshwater influenced shelves. Biogeosci. 6, 2421–2432. https://doi.org/10.5194/bg-6-2421-2009.

Chierici, M., Fransson, A., Anderson, L.G., 1999. Influence of m-cresol purple indicator additions on the pH of seawater samples: correction factors evaluated from a chemical speciation model. Mar. Chem. 65, 281–290. https://doi.org/10.1016/S0304-42039900020-1.

Chierici, M., Fransson, A., Lansard, B., Miller, L.A., Mucci, A., Shadwick, E., Thomas, H., Tremblay, J.E., Papakyriakou, T.N., 2011. Impact of biogeochemical processes and environmental factors on the calcium carbonate saturation state in the Circumpolar Flaw Lead in the Amundsen Gulf, Arctic Ocean. J. Geophys. Res. 116 (C9), C00G09. https://doi.org/10.1029/2011JC007184.

Chierici, M., Vernet, M., Fransson, A., Børsheim, K.Y., 2019. Net Community Production and Carbon Exchange From Winter to Summer in the Atlantic Water Inflow to the Arctic Ocean. Front. Mar. Sci. 6, 528. https://doi.org/10.3389/fmars.2019.00528.
Comeau, S., Gorsky, G., Jeffree, R., Teyssie, J.L., Gatusso, J.P., 2009. Impact of ocean acidification on a key Arcticpelagic mollusc *Limacina helicina*. Biogeosci. 6, 1877–1882. https://doi.org/10.5194/bg-6-1877-2009.
Cottier, F.R., Tverberg, V., Inall, M.E., Svendsen, H., Nilsen, F., Griffiths, C., 2005. Water mass modification in an Arctic fjord through cross shelf exchange: the seasonal hydrography of Kongsfjorden. Svalbard. J. Geophys. Res. 110, C12005. https://doi.org/10.1029/2004JC002757.
Cooper, L.W., McClelland, J.W., Holmes, R.M., Raymond, P.A., Gibson, J.J., Guay, C.K., Peterson, B.J., 2008. Flow-weighted values of runoff tracers d18O, DOC, Ba, alkalinity from the six largest Arctic rivers. Geophys. Res. Lett. 35, L18606. https://doi.org/10.1029/2008GL035007.
Dickson, A.G., Millero, F.J., 1987. A comparison of the equilibrium constants for the dissociation of carbonic acid in seawater media. Deep Sea Res. A 3410, 1733–1743. https://doi.org/10.1016/0198-01498790021-5.
Dickson, A.G., Sabine, C.L., Christian, J.R. (Eds.), 2007. Guide to best practices for ocean CO2 measurements. PICES Special Publication 3, pp. 191.
Dieckmann, G., Nehrke, G., Uhlig, C., Göttlicher, J., Gerland, S., Granskog, M.A., Thomas, D.N., 2010. Ikaite CaCO3. 6H2O discovered in Arctic sea ice. The Cryosphere 4, 227–230.
Doney, S.C., Balch, W.M., Fabry, V.J., Feely, R.A., 2009. Ocean acidification: A critical emerging problem for the ocean sciences. Oceanography 224, 16–25.
Ericson, Y., Ulfsbo, A., van Heuven, S., Kattner, G., Anderson, L.G., 2014. Increasing carbon inventory of the intermediate layers of the Arctic Ocean. J. Geophys. Res. Oceans 1194, 2312–2326. https://doi.org/10.1002/2013JC009514.
Ericson, Y., Falck, E., Chierici, M., Fransson, A., Kristiansen, S., Platt, S.M., Hermansen, O., Myhre, C.L., 2018. **Temporal variability in surface water pCO_2 in Adventfjorden West Spitsbergen with emphasis on physical and biogeochemical drivers**. J. Geophys. Res. Oceans 123, 4888–4905. https://doi.org/10.1029/2018JC014073.
Ericson, Y., Falck, E., Chierici, M., Fransson, A., Kristiansen, S., 2019a. Marine CO_2 system variability in a high arctic tidewater-glacier fjord system, Tempelfjorden. Svalbard. Cont. Shelf Res. 181, 1–13. https://doi.org/10.1016/j.csr.2019.04.013.
Ericson, Y., Chierici, M., Falck, E., Fransson, A., Jones, E.M., Kristiansen, S., 2019b. Seasonal dynamics of the marine CO_2 system in Adventfjorden, a West Spitsbergen fjord. Polar Res. 38, 3345. https://doi.org/10.33265/polar.v38.3345.
Ewertowski, M., 2014. Recent transformations in the High-Arctic glacier landsystem, Ragnabreen, Svalbard. Geografiska Annaler Series A 96, 265–285. https://doi.org/10.1111/geoa.12049.
Fabry, V., Mcclintock, J., Mathis, J., Grebmeier, J., 2009. Ocean Acidification at High Latitudes: The Bellwether. Oceanography 224, 160–171.
Feely, R.A., Sabine, C.L., Lee, K., Berelson, W., Kleypas, J., Fabry, V.J., Millero, F.J., 2004. Impact of anthropogenic CO_2 on the $CaCO_3$ system in the oceans. Science 3055682, 362–366. https://doi.org/10.1126/science.1097329.
Fer, I., Müller, M., Peterson, A.K., 2015. Tidal forcing, energetics, and mixing near the Yermak Plateau. Ocean Sci. 11, 287–304. https://doi.org/10.5194/os-11-287-2015.
Fransson, A., Chierici, M., Anderson, L.G., Bussmann, I., Kattner, G., Jones, E.P., Swift, J. H., 2001. The importance of shelf processes for the modification of chemical constituents in the waters of the Eurasian Arctic Ocean: implication for carbon fluxes. Cont. Shelf Res. 21 (3), 225–242. https://doi.org/10.1016/S0278-4343(00)00088-1.
Fransson, A., Chierici, M., Miller, L.A., Carnat, G., Shadwick, E., Thomas, H., Pineault, S., Papakyriakou, T.N., 2013. Impact of sea-ice processes on the carbonate system and ocean acidification at the ice-water interface in the Arctic Ocean. J. Geophys. Res. Oceans 118, 1–23. https://doi.org/10.1002/2013JC009164.
Fransson, A., Chierici, M., Nomura, D., Granskog, M.A., Kristiansen, S., Martma, T., Nehrke, G., 2015. Effect of glacial drainage water on the CO_2 system and ocean acidification state in an Arctic tidewater-glacier fjord during two contrasting years. J. Geophys. Res. Oceans 120. https://doi.org/10.1002/2014JC010320.
Fransson, A., Chierici, M., Hop, H., Findlay, H.S., Kristiansen, S., Wold, A., 2016. Late winter-to- summer change in ocean acidification state in Kongsfjorden, with implications for calcifying organisms. Polar Biol. 3910, 1841–1857. https://doi.org/10.1007/s00300-016-1955-5.
Fransson, A., Chierici, M., Nomura, D., Granskog, M.A., Kristiansen, S., Martma, T., Nehrke, G., 2020. Influence of glacial water and carbonate minerals on wintertime sea-ice biogeochemistry and the CO_2 system in an Arctic fjord in Svalbard. Ann. Glaciol. 1–21. https://doi.org/10.1017/aog.2020.52.
Fransson, A., Chierici, M., Skjelvan, I., Olsen, A., Assmy, P., Peterson, A., Spreen, G., Ward, B., 2017. Effect of sea-ice and biogeochemical processes and storms on under-ice water fCO_2 during the winter-spring transition in the high Arctic Ocean: implications for sea-air CO_2 fluxes. J. Geophys. Res. Oceans 122, 5566–5587. https://doi.org/10.1002/2016JC012478.
Frigstad, H., Andersen, T., Bellerby, R.G.J., Silyakova, A., Hessen, D.O., 2014. Variation in the seston C: N ratio of the Arctic Ocean and pan-Arctic shelves. J. Mar. Sys. 129, 214–223. https://doi.org/10.1016/j.jmarsys.2013.06.004.
Friis, K., Körtzinger, A., Wallace, D.W.R., 2003. The salinity normalization of marine inorganic carbon chemistry data. Geophys. Res. Lett. 30, 1085. https://doi.org/10.1029/2002GL015898.
González-Pola, C., Larsen, K.M.H., Fratantoni, P., Beszczynska-Möller, A. (Eds.). ICES Report on Ocean Climate 2018. ICES Cooperative Research Report No. 349, pp. 122.
Grasshof, K., Kremling, K., Ehrhardt, M., 2009. Methods of Seawater Analysis, 3rd ed. John Wiley, New York.
Hegseth, E.N., Sundfjord, A., 2008. Intrusion and blooming of Atlantic phytoplankton species in the high Arctic. J. Mar. Syst. 74, 108–119.
Henley, S.F., Porter, M., Hobbs, L., Braun, J., Guillaume-Castel, R., Venables, E.J., Dumont, E., Cottier, F., 2020. Nitrate supply and uptake in the Atlantic Arctic sea ice zone: seasonal cycle, mechanisms and drivers. Phil. Trans. Royal Soc. A 3782181, 20190361. https://doi.org/10.1098/rsta.2019.0361.
Hopwood, M.J., Carroll, D., Dunse, T., Hodson, A., Holding, J.M., Iriarte, J.L., Ribeiro, S., Achterberg, E.P., Cantoni, C., Carlson, D.F., Chierici, M., 2020. How does glacier discharge affect marine biogeochemistry and primary production in the Arctic? The Cryosphere 14, 1347–1383. https://doi.org/10.5194/tc-14-1347-2020.
Ingvaldsen, R.B., Bucklin, A., Fauchald,P., Gjøsæter, H., Haug, T., Jørgensen, L.L., Knutsen, T., Naustvoll, L.J., Wiebe. P., 2016. Cruise report SI_ARCTIC/Arctic Ecosystem survey R/V Helmer Hanssen, 19 August-7 September 2014. Toktrapport/Havforskningsinstituttet. 11–2016.
Ingvaldsen, R.B., Bucklin, A., Chierici, M., Gjøsæter, H., Haug, T., Hosia, A., Jørgensen, L. L., Knutsen, T., Naustvoll, L.J., Ona, E., Wiebe, P., 2016. Cruise Report SI_ARCTIC/Arctic Ecosystem Survey R/V Helmer Hanssen, 17 August-7 September 2015. Toktrapport/Havforskningsinstituttet. 14–2016.
Ingvaldsen, R.B., Gjøsæter, H., Hallfredsson, E., Haug, T., Hosia, A., Jørgensen, L.L., Knutsen, T., Lødemel, H.H., Menze, S., Naustvoll, L.J., 2017. Cruise report SI_ARCTIC/Arctic Ecosystem Survey R/V Helmer Hanssen, 2-16 September 2016. Toktrapport/Havforskningsinstituttet. 1–2017.
Ingvaldsen, R.B., Gjøsæter, H., Haug, T., Jørgensen, L.L., Knutsen, T., Lødemel, H.H., Menze, S., Naustvoll, L.J, Wiebe, P., 2017. Cruise report SI_ARCTIC/Arctic Ecosystem Survey R/V Helmer Hanssen, 21 August-7 September 2017. Toktrapport/Havforskningsinstituttet. 5-2017.
Ivanov, V., Smirnov, A., Alexeev, V., Koldunov, N.V., Repina, I., Semenov, V., 2018. Contribution of Convection-Induced Heat Flux to Winter Ice Decay in the Western Nansen Basin. J. Geophys. Res. 123 (9), 6581–6659. https://doi.org/10.1029/2018JC013995.
Jakobsson, M., Mayer, L., Coakley, B., Dowdeswell, J.A., Forbes, S., Fridman, B., Hodnesdal, H., Noormets, R., Pedersen, R., Rebesco, M., Schenke, H.W., Zarayskaya, Y., Accettella, D., Armstrong, A., Anderson, R.M., Bienhoff, P., Camerlenghi, A., Church, I., Edwards, M., Gardner, J.V., Hall, J.K., Hell, B., Hestvik, O., Kristoffersen, Y., Marcussen, C., Mohammad, R., Mosher, D., Nghiem, S. V., Pedrosa, M.T., Travaglini, P.G., Weatherall, P., 2012. The International Bathymetric Chart of the Arctic Ocean IBCAO Version 3.0. Geophys. Res. Lett. 39, 1–6. https://doi.org/10.1029/2012GL052219.
Johnson, K.M., Sieburth, J.M., Williams, P.J.L., Brändström, L., 1987. Coulometric total carbon dioxide analysis for marine studies - automation and calibration. Mar. Chem. 21, 117–133. https://doi.org/10.1016/0304-42038790033-8.
Kattner, G., Becker, H., 1991. Nutrients and organic nitrogenous compounds in the marginal ice zone of the Fram Strait. J. Mar. Syst. 2, 385–394. https://doi.org/10.1016/0924-79639190043-T.
Le Fouest, V., Postlethwaite, C., Morales Maqueda, M.A., Bélanger, S., Babin, M., 2011. On the role of tides and strong wind events in promoting summer primary production in the Barents Sea. Cont. Shelf Res. 31, 1869–1879. https://doi.org/10.1016/j.csr.2011.08.013.
Leu, E., Søreide, J.E., Hessen, D.O., Falk-Petersen, S., Berge, J., 2011. Consequences of changing sea-ice cover for primary and secondary producers in the European Arctic shelf seas: timing, quantity, and quality. Prog. Oceanogr. 90, 18–32. https://doi.org/10.1016/j.pocean.2011.02.004.
Lewis, E., Wallace, D.W.R., 1998. Program developed for CO_2 system calculations. ORNL/CDIAC-105, Carbon Dioxide Information Analysis Center, Oak Ridge National Laboratory, Oak Ridge, Tennessee.
Lind, S., Ingvaldsen, R.B., Furevik, T., 2018. Arctic warming hotspot in the northern Barents Sea linked to declining sea-ice import. Nat. Clim. Chang. 8, 634–639. https://doi.org/10.1038/s41558-018-0205-y.
Lischka, S., Riebesell, U., 2012. Synergistic effects of ocean acidification and warming on overwintering pteropods in the Arctic. Glob. Chang. Biol. 18, 3517–3528. https://doi.org/10.1111/gcb.12020.
Loose, B., McGillis, W.R., Schlosser, P., Perovich, D., Takahashi, T., 2009. Effects of freezing, growth, and ice cover on gas transport processes in laboratory seawater experiments. Geophys. Res. Lett. 36, L05603. https://doi.org/10.1029/2008GL036318.
Mehrbach, C., Culberson, C.H., Hawley, J.E., Pytkowicz, R.M., 1973. Measurement of the apparent dissociation constants of carbonic acid in seawater at atmospheric pressure. Limnol. Oceanogr. 18, 897–907. https://doi.org/10.4319/lo.1973.18.6.0897.
Menze, S., Ingvaldsen, R.B., Haugan, P., Fer, I., Sundfjord, A., Beszczynska-Moeller, A., Falk-Petersen, S., 2019. Atlantic water pathways along the north-western Svalbard shelf mapped using vessel-mounted current profilers. J. Geophys. Res. Oceans 1243, 1699–1716. https://doi.org/10.1029/2018JC014299.
Millero, F.J., Leung, W.H., 1976. Thermodynamics of Seawater at One Atmosphere. Am. J. Sci. 2769, 1035–1077. https://doi.org/10.2475/ajs.276.9.1035.
Millero, F.J., 2007. The marine inorganic carbon cycle. Chem. Rev. 107, 308–341. https://doi.org/10.1021/cr0503557.
Mucci, A., 1983. The solubility of calcite and aragonite in seawater at various salinities, temperatures, and one atmosphere total pressure. Am. J. Sci. 283, 780–799.
Neukermans, G., Oziel, L., Babin, M., 2018. Increased intrusion of warming Atlantic water leads to rapid expansion of temperate phytoplankton in the Arctic. Glob. Change Biol. 24, 2545–2553. https://doi.org/10.1111/gcb.14075.
Onarheim, I.H., Smedsrud, L.H., Ingvaldsen, R.B., Nilsen, F., 2014. Loss of sea ice during winter north of Svalbard. Tellus A 661, 23933. https://doi.org/10.3402/tellusa.v66.23933.
Orr, J.C., Fabry, V.J., Aumont, O., Bopp, L., Doney, S.C., Feely, R.A., Gnanadesikan, A., Gruber, N., Ishida, A., Joos, F., Key, R.M., Lindsay, K., Maier-Reimer, E., Matear, R., Monfray, P., Mouchet, A., Najjar, R.G., Plattner, G.-K., Rodgers, K.B., Sabine, C.L., Sarmiento, J.L., Schlitzer, R., Slater, R.D., Totterdell, I.J., Weirig, M.-F.,

Yamanaka, Y., Yool, A., 2005. Anthropogenic ocean acidification over the twenty-first century and its impact on calcifying organisms. Nature 437, 681–686. https://doi.org/10.1038/nature04095.
Oziel, L., Neukermans, G., Ardyna, M., Lancelot, C., Tison, J.-L., Wassmann, P., Sirven, J., Ruiz-Pino, D., Gascard, J.-C., 2017. Role for Atlantic inflows and sea ice loss on shifting phytoplankton blooms in the Barents Sea. J. Geophys. Res. 122, 5121–5139. https://doi.org/10.1002/2016JC012582.
Oziel, L., Baudena, A., Ardyna, M., Massicotte, P., Randelhoff, A., Sallée, J.B., Ingvaldsen, R.B., Devred, E., Babin, M., 2020. Faster Atlantic currents drive poleward expansion of temperate phytoplankton in the Arctic Ocean. Nature commun. 11, 1–8. https://doi.org/10.1038/s41467-020-15485-5.
Pérez-Hernández, M.D., Pickart, R.S., Pavlov, V., Våge, K., Ingvaldsen, R., Sundfjord, A., Renner, A.H.H., Torres, D.J., Erofeeva, S.Y., 2017. The Atlantic Water boundary current north of Svalbard in late summer. J. Geophys. Res. Ocean. 122, 2269–2290. https://doi.org/10.1002/2016JC012486.
Pierrot, D., Lewis, E., Wallace, D.W.R., 2006. MS Excel program developed for CO_2 system calculations. In: Rep. ORNL/CDIAC-105a. Carbon Dioxide Inf. Anal. Cent., Oak Ridge Natl. Lab., US Department of Energy, Oak Ridge, TN.
Polyakov, I.V., Pnyushkov, A.V., Alkire, M.B., Ashik, I.M., Baumann, T.M., Carmack, E. C., Goszczko, I., Guthrie, J., Ivanov, V.V., Kanzow, T., Krishfield, R., Kwok, R., Sundfjord, A., Morison, J., Rember, R., Yulin, A., 2017. Greater role for Atlantic inflows on sea-ice loss in the Eurasian Basin of the Arctic Ocean. Science 356 (6335), 285–291. https://doi.org/10.1126/science.aai8204.
Raimondi, L., Matthews, J.B.R., Atamanchuk, D., Azetsu-Scott, K., Wallace, D.W., 2019. The internal consistency of the marine carbon dioxide system for high latitude shipboard and in situ monitoring. Marine Chemistry 213, 49–70. https://doi.org/10.1016/j.marchem.2019.03.001.
Rainville, L., Lee, C.M., Woodgate, R.A., 2011. Impact of wind-driven mixing in the Arctic Ocean. Oceanography 24, 136–145. https://doi.org/10.5670/oceanog.2011.65.
Randelhoff, A., Sundfjord, A., Reigstad, M., 2015. Seasonal variability and fluxes of nitrate in the surface waters over the Arctic shelf slope. Geophys. Res. Lett. 3442–3449 https://doi.org/10.1002/2015GL063655.
Randelhoff, A., Reigstad, M., Chierici, M., Sundfjord, A., Ivanov, V., Cape, M.R., Vernet, M., Tremblay, J.-E., Bratbak, G., Kristiansen, S., 2018. Seasonality of the physical and biogeochemical hydrography in the inflow to the Arctic Ocean through Fram Strait. Front. Mar. Sci. 5, 1–16.
Redfield, A.C., Ketchum, B.H., Richards, F.A., 1963. The influence of organisms on the composition of sea-water. In: Hill, M.N. (Ed.), The Sea: Ideas and Observations on the Progress in the Study of the Sea. Interscience, New York, pp. 26–77.
Reigstad, M., Wassmann, P., Riser, C.W., Øygarden, S., Rey, F., 2002. Variations in hydrography, nutrients and chlorophyll a in the marginal ice-zone and the central Barents Sea. J. Mar. Syst. 38, 9–29. https://doi.org/10.1016/S0924-79630200167-7.
Renner, A.H.H., Sundfjord, A., Janout, M.A., Ingvaldsen, R.B., Beszczynska-Möller, A., Pickart, R.S., Pérez-Hernández, M.D., 2018. Variability and redistribution of heat in the Atlantic water boundary current north of Svalbard. J. Geophys. Res. Ocean. 123 (9), 6373–6391. https://doi.org/10.1029/2018JC013814.
Rudels, B., Björk, G., Nilsson, J., Winsor, P., Lake, I., Nohr, C., 2005. The interaction between waters from the Arctic Ocean and the Nordic Seas north of Fram Strait and along the East Greenland Current: Results from the Arctic Ocean-02 Oden expedition. J. Mar. Syst. 55, 1–30. https://doi.org/10.1016/j.jmarsys.2004.06.008.
Rudels, B., Korhonen, M., Schauer, U., Pisarev, S., Rabe, B., Wisotzki, A., 2015. Circulation and transformation of Atlantic water in the Eurasian Basin and the contribution of the Fram Strait inflow branch to the Arctic Ocean heat budget. Prog. Oceanogr. 132, 128–152. https://doi.org/10.1016/j.pocean.2014.04.003.
Rysgaard, S., Glud, R.N., Sejr, M.K., Bendtsen, J., Christensen, P.B., 2007. Inorganic carbon transport during sea ice growth and decay: a carbon pump in polar seas. J. Geophys. Res. 112, C03016. https://doi.org/10.1029/2006JC003572.
Rysgaard, S., Glud, R.N., Lennert, K., Cooper, M., Halden, N., Leakey, R.J.G., Hawthorne, F.C., Barber, D., 2012. Ikaite crystals in melting sea ice – implications for pCO_2 and pH levels in Arctic surface waters. The Cryosphere 6, 901–908. https://doi.org/10.5194/tc-6-901-2012.
Sakshaug, E., 2004. Primary and secondary production in the Arctic Seas. In: Stein, R., Macdonald, R.W. (Eds.), The organic carbon cycle in the Arctic Ocean. Springer, Berlin, Germany, pp. 57–81.
Schlitzer, R., 2015. Ocean Data View. http://www.odw.awi.de.
Semiletov, I.P., Makshtas, A., Akasofu, S.-I., 2004. Atmospheric CO_2 balance: The role of Arctic sea ice. Geophys. Res. Lett. 31, L05121. https://doi.org/10.1029/2003GL017996.
Shadwick, E.H., Thomas, H., Chierici, M., Else, B., Fransson, A., Michel, C., Miller, L.A., Mucci, A., Niemi, A., Papakyriakou, T.N., Tremblay, J.-E., 2011. Seasonal variability of the organic carbon system in the Amundsen Gulf region of the southeastern Beaufort Sea. Limnol. Oceanogr. 561, 303–322. https://doi.org/10.4319/lo.2011.56.1.0303.
Sievaag, A., Fer, I., 2009. Early Spring oceanic heat fluxes and mixing observed from drift stations North of Svalbard. J. Phys. Oceanogr. 3912, 3049–3069. https://doi.org/10.1175/2009JPO4172.1.
Slagstad, D., Wassmann, P.F.J., Ellingsen, I., 2015. Physical constrains and productivity in the future Arctic Ocean. Front. Mar. Sci. 2, 1–23. https://doi.org/10.3389/fmars.2015.00085.
Søreide, J.E., Leu, E., Berge, J., Graeve, M., Falk-Petersen, S., 2010. Timing of blooms, algal food quality and Calanus glacialis reproduction and growth in a changing Arctic. Glob. Chang. Biol. 16, 3154–3163. https://doi.org/10.1111/j.1365-2486.2010.02175.x.
Spall, M.A., 2013. On the circulation of Atlantic Water in the Arctic Ocean. J. Phys. Oceanogr. 43, 2352–2371. https://doi.org/10.1175/JPO-D-13-079.1.
Spreen, G., Kaleschke, L., Heygster, G., 2008. Sea ice remote sensing using AMSR-E 89-GHz channels. J. Geophys. Res. 113, C02S03. https://doi.org/10.1029/2005JC003384.
Stöven, T., Tanhua, T., Hoppema, M., von Appen, W.-J., 2016. Transient tracer distributions in the Fram Strait in 2012 and inferred anthropogenic carbon content and transport. Ocean Sci. 12, 319–333. https://doi.org/10.5194/os-12-319-2016.
Takahashi, T., Olafsson, J., Goddard, J.G., Chipman, D.W., Sutherland, S.C., 1993. Seasonal variation of CO_2 and nutrients in the high latitude surface oceans: A comparative study. Glob. Biogeochem. Cycles 74, 843–878. https://doi.org/10.1029/93GB02263.
Torres-Valdés, S., Tsubouchi, T., Bacon, S., Naveira-Garabato, A.C., Sanders, R., McLaughlin, F.A., Petrie, B., Kattner, G., Azetsu-Scott, K., Whitledge, T.E., 2013. Export of nutrients from the Arctic Ocean. J. Geophys. Res. Oceans 118, 1625–1644. https://doi.org/10.1002/jgrc.20063.
Tremblay, J.E., Anderson, L.G., Matrai, P., Coupel, P., Belanger, S., Michel, C., Reigstad, M., 2015. Global and regional drivers of nutrient supply, primary production and CO2 drawdown in the changing Arctic Ocean. Prog. Oceanogr. 139, 171–196. https://doi.org/10.1016/j.pocean.2015.08.009.
Tsubouchi, T., Våge, K., Hansen, B., Larsen, K.M.H., Østerhus, S., Johnson, C., Jónsson, S., Valdimarsson, H., 2020. Increased ocean heat transport into the Nordic Seas and Arctic Ocean over the period 1993–2016. Nat. Clim. Chang. https://doi.org/10.1038/s41558-020-00941-3.
Ulfsbo, A., Jones, E.M., Casacuberta, N., Korhonen, M., Rabe, B., Karcher, M., van Heuven, S.M.A.C., 2018. Rapid changes in anthropogenic carbon storage and ocean acidification in the intermediate layers of the Eurasian Arctic Ocean, 1996–2015. Glob. Biogeochem. Cycles 32, 1254–1275. https://doi.org/10.1029/2017GB005738.
van Heuven, S., Pierrot, D., Rae, J.W.B., Lewis, E., Wallace, D.W.R., 2011. MATLAB program developed for CO_2 system calculations. ORNL/CDIAC-105b, Carbon Dioxide Information Analysis Center, Oak Ridge National Laboratory, Oak Ridge, Tennessee. http://dx.doi.10.3334/CDIAC/otg.CO2SYS_MATLAB_v1.1.
Wanninkhof, R., 2014. Relationship between wind speed and gas exchange over the ocean revisited. Limnol. Oceanogr. Methods 126, 351–362. https://doi.org/10.4319/lom.2014.12.351.
Wassmann, P. Friedrich, Reigstad, M., Haug, T., Rudels, B., Carroll, M., Hop, H., Wing-Gabrielsen, G., Falk-Petersen, S., Denisenko, S.G., Arashkevich, E., Slagstad, D., Pavlova, O., 2006. Food webs and carbon flux in the Barents Sea. In Structure and function of contemporary food webs on Arctic shelves: a panarctic comparison. Prog. Ocean. 71, 2–4. https://doi.org/10.1016/j.pocean.2006.10.0.
Wassmann, P., Reigstad, M., 2011. Future Arctic Ocean seasonal ice zones and implications for pelagic-benthic coupling. Oceanography 24, 220–231. https://doi.org/10.5670/oceanog.2011.74.
Weiss, R.F., 1974. Carbon dioxide in water and seawater: the solubility of a non-ideal gas. Mar. Chem. 23, 203–205. https://doi.org/10.1016/0304-42037490015-2.
Wolf-Gladrow, D.A., Zeebe, R.E., Klaas, C., Körtzinger, A., Dickson, A.G., 2007. Total alkalinity: The explicit conservative expression and its application to biogeochemical processes. Mar. Chem. 1061–2, 287–300. https://doi.org/10.1016/j.marchem.2007.01.006.
Woosley, R.J., Millero, F.J., Takahashi, T., 2017. Internal consistency of the inorganic carbon system in the Arctic Ocean. Limnol. Oceanogr. Methods 1510, 887–896. https://doi.org/10.1002/lom3.10208.
Yamamoto-Kawai, M., McLaughlin, F.A., Carmack, E.C.S., Nishino, S., Shimada, K., 2009. Aragonite undersaturation in the Arctic Ocean: Effects of ocean acidification and sea ice melt. Science 326, 1098–1100. https://doi.org/10.1126/science.1174190.
Yamamoto-Kawai, M., McLaughlin, F.A., Carmack, E.C., 2011. Effects of ocean acidification, warming and melting of sea ice on aragonite saturation of the Canada Basin surface water. Geophys. Res. Lett. 38, L03601. https://doi.org/10.1029/2010GL045501.
Zeebe, R.E., Wolf-Gladrow, D., 2001. CO_2 in Seawater: Equilibrium, Kinetics, Isotopes. Elsevier, Amsterdam, p. 346.
Zhang, Y., Yamamoto-Kawai, M., Williams, W.J., 2020. Two decades of ocean acidification in the surface waters of the Beaufort Gyre, Arctic Ocean: Effects of sea ice melt and retreat from 1997–2016. Geophys. Res. Lett. 47, e60119 https://doi.org/10.1029/2019GL086421.